

# FINAL PUBLISHABLE REPORT

Grant Agreement number                    17FUN06  
 Project short name                            SIQUEST  
 Project full title                              Single-photon sources as new quantum standards

Project start date and duration:		01 June 2018, 42 months
Coordinator: Stefan Kück, PTB		Tel: +49 531 5924010
Project website address: <a href="https://www.siqust.eu/">https://www.siqust.eu/</a>		E-mail: stefan.kueck@ptb.de
Internal Funded Partners:	External Funded Partners:	Unfunded Partners:
1 PTB, Germany	8 CNR, Italy	
2 Aalto, Finland	9 CSIC, Spain	
3 CMI, Czech Republic	10 FAU, Germany	
4 INRIM, Italy	11 INFN, Italy	
5 Metroserf, Estonia	12 TUB, Germany	
6 NPL, United Kingdom	13 UdS, Germany	
7 VTT, Finland	14 UNITO, Italy	
	15 USTUTT, Germany	
RMG: -		

## TABLE OF CONTENTS

1	Overview .....	3
2	Need .....	3
3	Objectives .....	3
4	Results .....	4
4.1	Objective 1 .....	4
4.1.1	Single-photon sources based on impurity centres in nano and bulk diamonds .....	4
4.1.2	Single-photon sources based on semiconductor quantum dots .....	5
4.1.3	Single-photon sources based on molecules .....	8
4.1.4	Summary .....	10
4.2	Objective 2 .....	11
4.2.1	2D materials based on hexagonal boron nitride and transition metal dichalcogenides .....	11
4.2.2	Coupling designs to optimise the collection efficiency - Single molecules in solid-state matrices ...	12
4.2.3	Coupling schemes for quantum dots and the impact of excitation schemes on the quantum optical properties of single-photon sources .....	14
4.3	Objective 3 .....	21
4.3.1	Sources of indistinguishable and entangled photons based on near infrared (< 1 $\mu\text{m}$ ) quantum dot single-photon sources .....	21
4.3.2	Perspectives of sources of indistinguishable and entangled photons based on single photon sources in metrology .....	26
4.3.3	Novel sensing and measurement techniques .....	26
4.3.4	Summary .....	27
4.4	Objective 4 .....	27
4.4.1	Low optical flux detectors (LOFP) .....	27
4.4.2	Predictable quantum efficient detector for traceable low optical flux measurements of SPS systems	27
4.4.3	Transmission-type photodetectors as an alternative attenuator to achieve and monitor low photon flux	28
4.4.4	Single-photon source characterisation facilities .....	29
4.4.5	Transportable single photon sources .....	33
4.4.6	Detection efficiency comparison .....	35
4.4.7	$g(2)$ -comparison using Hanbury Brown Twiss interferometer .....	36
4.4.8	Summary and outlook .....	37
5	Impact .....	37
6	List of publications .....	38
7	Contact details .....	41

## 1 Overview

The aim of this project was to develop new absolute standard radiation sources, which exploit the discrete and quantum nature of photons, and the necessary metrological infrastructure. These sources were based on single-photon emitters with a calculable photon emission rate and high purity, i.e. with a very low multiple photon emission probability. Such sources can now be used as new quantum standards for a large number of applications, e.g. for use in the calibration of single-photon detectors, for the realisation of the SI base unit candela, for quantum random number generation, for quantum key distribution, for subshot noise metrology, for quantum enhanced metrology, and for photon-based quantum computation.

Single-photon sources for different kinds of applications have been further developed with respect to higher photon rates, higher purity and smaller emission bandwidths. Some of these sources are now used for the calibration of single-photon detectors and will soon be used in quantum key distribution testbeds and for sub shot noise metrology. Despite this progress, stability, reliability and performance still needs to be increased by engineering all aspects involved in single-photon sources (material development, optics, pumping schemes etc.). Metrological infrastructure has been developed in different NMIs, who are now able to characterise single-photon sources in a more sophisticated way. In conclusion, user needs have been addressed, however, there is still the need for improvement.

## 2 Need

Single-photon sources are needed for applications in quantum technologies such as quantum computing, quantum communications, quantum metrology, quantum enhanced imaging and sensing), which are amongst the most relevant topics with respect to innovation and technology in Europe. This importance can be seen in the EC's 1 billion € "Quantum Flagship" programme that started in 2018. This programme was triggered by the "Quantum Manifesto" and related European and national programmes.

The use of single-photon sources in quantum computing should lead to much needed increases in computational power, however, the same use of quantum computing will also mean that the currently safe cryptographic procedures that are used in communication and data storage will become obsolete. Thus, quantum cryptography, quantum key distribution and quantum communication need to be further developed to maintain data safety and security. Further to this, quantum metrology is needed to enable the classical shot-noise limit to be undercut in order to support an increased precision in measurements. In addition, quantum imaging and quantum sensing needed to be developed to enable high resolution measurements, and the ability to perform imaging without the direct detection of photons.

An ideal single-photon source emits one photon on demand, at a time chosen by the user with the emitted photons being indistinguishable from one another and having an adjustable repetition rate. Such a photon source was greatly needed as it represented a new quantum standard with an extensive range of widely needed applications: for the calibration of single photon counter devices, for the realisation of the SI base unit candela, for quantum random number generation, for quantum key distribution, for photon based quantum computation and subshot noise metrology.

Furthermore, the characteristics of the single-photon sources needed to be measured with traceability to national standards, therefore the necessary measurement infrastructure for traceable single-photon source characterisation needed to be developed.

Significant progress was made in the previous EMRP project EXL02 SIQUTE, where e.g. for the first time a single-photon source was metrologically characterised. However, the photon fluxes of state-of-the-art technologies were too low ( $< 1 \times 10^6$  photons per second) and the emission bandwidths were too broad ( $> 100$  nm) for practical use of this single-photon source. Therefore, further work was needed to develop close-to-ideal single-photon sources.

## 3 Objectives

This project focused on the development of single-photon sources as new quantum standards. The specific objectives were:

1. To develop single-photon sources as new quantum standards in the visible, near infrared and telecom wavelength range, based on optically and electrically driven impurity centres in nano and bulk diamonds, quantum dots (QD) in semiconductor structures and molecules having, simultaneously, photon rates  $> 1 \times 10^6$  photons per second, emission bandwidths  $< 2$  nm and high purity emission indicated by  $g^{(2)}(t=0)$  values  $< 0.05$ .
2. To assess new materials and concepts for single-photon sources, such as 2D materials (e.g. hexagonal boron nitride and thin transition metal dichalcogenides) and coupling designs to

optimise the collection efficiency (e.g. micro-resonators, waveguides, optical antennas). To assess the impact of excitation schemes on the quantum optical properties of single-photon sources.

3. To establish sources of indistinguishable and entangled photons based on near infrared ( $< 1 \mu\text{m}$ ) QD single-photon sources with a visibility  $> 90 \%$  and novel sensing and measurement techniques based on these sources.
4. To develop metrology infrastructure for traceable single-photon source characterisation, i.e. detectors, amplifiers, single-photon spectroradiometers.
5. To promote the results, to trigger commercialisation of products, and to deliver input to standardisation organisations.

## 4 Results

In the following, a summary of the project's outputs, delivered against each of the project's objectives, will be presented.

### 4.1 Objective 1

*Development of single photon sources as new quantum standards in the visible, near infrared and telecom wavelength range, based on optically and electrically driven impurity centres in nano and bulk diamonds, QD in semiconductor structures and molecules having, simultaneously, photon rates  $> 1 \times 10^6$  photons per second, emission bandwidths  $< 2 \text{ nm}$  and high purity emission indicated by  $g^{(2)}(\tau = 0)$  values  $< 0.05$ .*

#### 4.1.1 Single-photon sources based on impurity centres in nano and bulk diamonds

Type-IIa diamond bulk crystals were implanted with ions (i.e., Sn, Pb, He, F, Cl, Er) that are supposed to be an efficient single-photon emitter. The samples were then spectroscopically characterised at room temperature in order to demonstrate the successful implantation of the ions.

Diamond samples implanted with Sn demonstrated single-photon emission at room temperature under 520 nm and 532 nm laser excitation. The Sn Vacancy (SnV) centre of the samples implanted with Sn exhibited single-photon purity ( $g^{(2)}(0)$  values) down to  $0.29 \pm 0.02$  with a saturation photon rate of approx.  $1.4 \times 10^6$  photons/s. Single-photon purity could be enhanced to a  $g^{(2)}(0)$  down to 0.05 but this was at the expense of the saturation photon rate, which was only  $0.15 \times 10^6$  photons/s. FAU, UdS and PTB found that nanofabrication of the diamond samples, in particular the etch steps required for thinning down the diamond to the required thickness of  $\ll 1 \mu\text{m}$ , introduces blinking of the colour centres and additional background fluorescence. Nevertheless, large single photon count rates (up to 500 kcps) at sufficient purity ( $g^{(2)}(0) \sim 0.2 \dots 0.4$ ) could be demonstrated from single SnV centres in an optical antenna.

The successful generation of GeV centres in diamond by implantation of Ge ions and annealing at  $1200 \text{ }^\circ\text{C}$ , carried out by INFN, INRIM and UNITO, has been shown and samples with Ge Vacancy (GeV) colour centres were characterised in terms of fluorescence mapping, photon rate, single-photon purity ( $g^{(2)}(0)$ -value) and spectral characteristics. Three GeV centres were characterised, and their spectral line emission (zero phonon line) was located at 604 nm, in Figure 1, a typical emission spectrum of a GeV-centre is shown. Plasma treatment and acid treatment were carried out to clean the diamond surface from contamination. The GeV sample was characterised at PTB in a confocal microscope setup that was built for this purpose. The setup is optimised for high transmission, i.e., a high numerical aperture (NA) microscope objective and high transmission spectral filters were implemented. At first, the single-photon purity obtained was approx. 0.5. Investigations at PTB showed that the background emission from the samples' surface was the most reasonable explanation for the  $g^{(2)}$  results. Background-corrected  $g^{(2)}$  values are largely between 0 and 0.3. Therefore, the sample was brought into an acid bath of 3:1 sulfuric acid (96 %) and nitric acid (70 %) to oxidise its surface and clean the sample of contamination. An improvement of non-corrected  $g^{(2)}$  values was reached, where most emitters now showed values below 0.5 afterwards. With one GeV-centre, a saturation count rate of  $N_{\text{sat}} = (265 \pm 65) \text{ kcps}$  was obtained, using the saturation model  $N(P) = \frac{N_{\text{sat}} P}{P + P_{\text{sat}}} + m P$ , where  $N$  is the count rate,  $P$  the excitation power,  $N_{\text{sat}} = (265 \pm 65) \text{ kcps}$  the saturation count rate,  $P_{\text{sat}} = (3.6 \pm 1.2) \text{ mW}$  the saturation laser power and  $m = (3.8 \pm 0.0) \frac{\text{kcps}}{\text{mW}}$  the linear background factor, see Figure 1. The measured  $g^{(2)}$  function was fitted using a standard three-level-scheme  $g^{(2)}$  function convoluted with a gaussian normal distribution representing the timing jitter of the detection system (SPADs + TimeTagger), see Figure 1. The resulting  $g^{(2)}$  value was  $0.14 \pm 0.04$ . The residual value of  $g^{(2)}$  can be fully attributed to the linear background from the sample. A possible origin of this background could be Raman scattering, as the second order Raman lines overlap with the GeV centre's emission for 532 nm excitation.

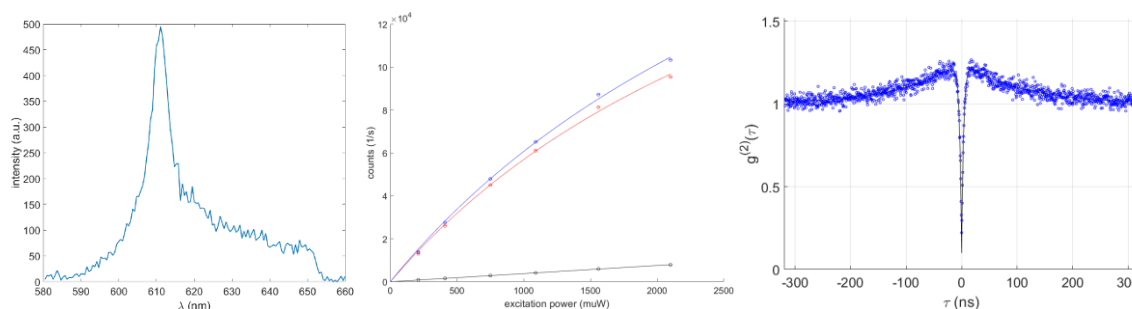


Figure 1. Left) Spectral distribution of a typical GeV centre's emission. The zero-phonon line of this GeV centre is at 610 nm and has a Full Width at a Half Maximum of 5 nm. The phonon sideband is cut-off for wavelength higher than 650 nm by the bandpass filter of the setup. Middle) Saturation measurement of a GeV centre. Blue: total counts, red: count due to GeV-centre emission, black: background. Right)  $g^{(2)}$  measurements of a GeV centre. The measured  $g^{(2)}$  function was fitted using a standard three-level-scheme  $g^{(2)}$  function convoluted with a gaussian normal distribution representing the timing jitter of the detection system.

The Pb Vacancy (PbV) centre of the samples implanted with Pb exhibited a single-photon purity  $g^2(0)$  value  $< 0.5$  after background noise correction, which originated from the first and second-order Raman scattering of diamond. Preliminary experiments also indicated anti-bunching behaviour from F-related centres.

In order to better understand the emission characteristics of impurity centres in nanodiamond, back focal plane imaging of the emission of a nitrogen-vacancy (NV)-centre at a dielectric interface was compared to theoretical models for the calculation of the angular emission patterns. The orientation of the NV-centres was obtained, from measurements of the fluorescence intensity, independently of the polarisation angle of the linearly polarised excitation laser. The collection efficiency was calculated to be higher than 80 % using the model of the angular emission of the NV-centres. This method is also applicable to other emitters like Si-vacancy centres, tin-vacancy centres, and hexagonal boron-nitride (hBN).

Metrosert, VTT and CMI developed an optical excitation scheme for impurity-centre based SPS-s.

#### 4.1.2 Single-photon sources based on semiconductor quantum dots

Two different types of structures for InGaAs, as single-photon emitters, were fabricated and investigated: microlens structures and mesa-type structures. In general, extraction efficiency of self-assembled semiconductor QDs is constrained due to the high refractive index contrast at the semiconductor to air interface. This can be overcome using either cavity systems or broadband approaches like microlenses, as it was done within this project. QD-microlenses emitting in the 930 nm have been realised deterministically by means of advanced in-situ electron beam lithography and plasma etching [1], see Figure 2. The single-photon emitter consists of an InGaAs QD deterministically embedded into a monolithic microlens, positioned on top of a distributed Bragg reflector. Numerical simulations of a similar geometrical configuration [2] predict an enhancement of the extraction efficiency of up to 23 %, when using a collecting lens with a numerical aperture (NA) of 0.7. An additional antireflection layer on top of the microlens surface further decreases the coupling losses. The fabrication process is described in detail in reference [3].

The mesa-type sample structure, shown in Figure 2, is grown by metal-organic chemical vapour deposition. First, 300 nm GaAs are deposited on a (001) GaAs substrate. Next, 23 pairs of AlGaAs and GaAs layers, with thicknesses of 78 nm and 67 nm, respectively, are forming a distributed Bragg reflector which reflects the light emitted into the lower hemisphere. A 67 nm thick spacer is grown on top, followed by a thin layer of self-assembled InGaAs QDs and a capping layer with a thickness of 420 nm. Suitable QDs at cryogenic temperatures are selected by cathodoluminescence spectroscopy, whereas electron-beam lithography (EBL) is used to form micromesas at the pre-selected positions. These mesas have a cylindrical shape with a radius

<sup>1</sup> M. Gschrey et al, Nature Communications 6, 7662 (2015)

<sup>2</sup> Gschrey M et al. 2015 Highly indistinguishable photons from deterministic quantum-dot microlenses utilizing three-dimensional in situ electron-beam lithography *Nat. Commun.* **6** 7662

<sup>3</sup> Schnauber P et al. 2016 Bright Single-Photon Sources Based on Anti-Reflection Coated Deterministic Quantum Dot Microlenses Technologies 4 1

between 600 nm and 640 nm and a height of 800 nm. For further information on the used in-situ EBL nanotechnology process, TUB refers to Ref. [4].

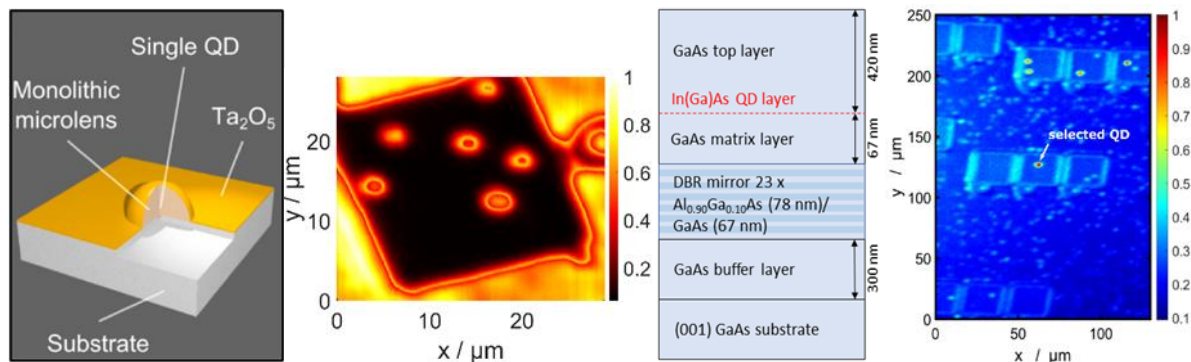


Figure 2. Left) Single InGaAs QD positioned in the centre of a monolithic microlens, covered with an antireflection coating to improve the extraction efficiency into the first lens of the setup. Taken from [3]. Middle-left) 2D micro-photoluminescence scan of the QD-microlens sample at 10 K. middle-right) Schematic of the sample structure. right) Micro-photoluminescence scan of the sample emission for emission wavelengths above 900 nm. The  $\mu$ PL intensity is significantly higher for QDs integrated into micromesas by in-situ EBL which nicely illustrates the enhancement of photon extraction by these nanophotonic structures.

First, a traceable single-photon source based on a non-resonantly driven InGaAs QD in a microlens structure with a spectral bandwidth of 42 pm (Full Width Half Maximum (FWHM)) and a single-photon purity corresponding to a  $g^{(2)}(0)$  value of  $0.24 \pm 0.06$  was realised. The highest optical power under non-resonant pulsed excitation with a repetition frequency of 80 MHz amounts to  $(79.4 \pm 1.2)$  fW (corresponding to approx.  $3.7 \times 10^5$  photons per second) for an emission wavelength of 922.4 nm. High optical power is achieved by extraction efficiency enhancement through monolithic microlenses and by low loss bandpass filtering, leading to a high setup transmission of  $(25.9 \pm 0.4)$  %. The setup is shown in Figure 3.

The photon flux stability of the source was analysed using the overlapping Allan deviation. Here, white noise dominates for short sampling times and a minimum deviation of 0.58 % is reached for averaging 92 values, each with an integration period of one second. This was the first absolutely characterised quantum dot based single-photon source emitting photons under pulsed excitation [5]. The triggered emission enables full control over the time interval between two consecutive photons, which can be used to tune the photon flux over a wide range without changing the saturation properties. Furthermore, PTB and CMI have demonstrated the feasibility of detector calibrations in the near infrared. The ratio of detection efficiencies of two similar SPAD detectors has been determined with a standard uncertainty of 0.7 %. This result has been confirmed with the standard double attenuator technique. The simultaneous count rate measurement as part of the relative calibration allows statistical uncertainties as low as 0.11 % to be reached due to the lack of dependence on the temporal stability of the photon flux. Moreover, the count rate ratio does not depend on the brightness of the single-photon source, as long as a sufficient signal-to-noise ratio can be reached.

<sup>4</sup> S. Rodt and S. Reitzenstein, "High-performance deterministic in situ electron-beam lithography enabled by cathodoluminescence spectroscopy," *Nano Ex.* 2, 014007 (2021).

<sup>5</sup> Georgieva, H.; López, M.; Hofer, H.; Christinck, J.; Rodiek, B.; Schnauber, P.; Kaganskiy, A.; Heindel, T.; Rodt, S.; Reitzenstein, S.; Kück, S. (2020): Radiometric characterization of a triggered narrow-bandwidth single-photon source and its use for the calibration of silicon single-photon avalanche detectors. In: *Metrologia* 57 055001. <https://doi.org/10.1088/1681-7575/ab9db6>

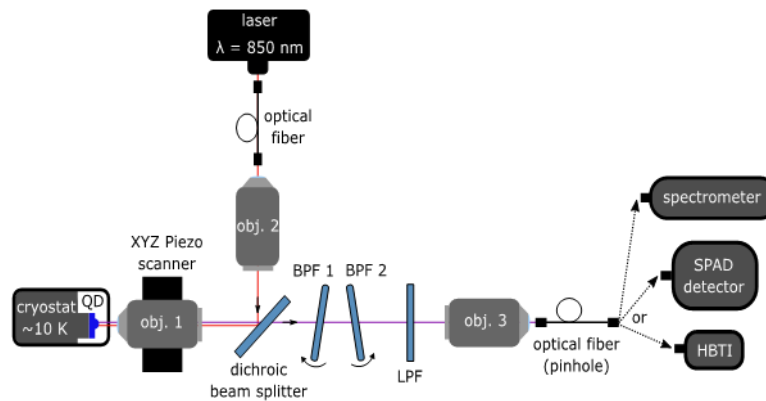


Figure 3. Schematic of the experimental setup for the optical characterisation of InGaAs QDs emitting in the near infrared.

For the investigation of a single-photon source based on mesa-like structures, further improvements were made to increase the collection efficiency, i.e., the setup transmission was improved by a factor of 2. Hence, TUB and PTB have developed a pulsed InGaAs QD based single-photon source applied for the direct calibration of a single-photon avalanche detector against a classical analogue reference detector, provided by CMI. The single-photon source was metrologically characterised with respect to its total radiant flux, which was up to  $2.55 \times 10^6$  photons/s, corresponding to 545 fW at an emission wavelength of  $\lambda = 929.8$  nm, and with a single-photon purity of  $g^{(2)}(0) < 0.25$  [6]. In Figure 4, the spectrum before and after spectral filtering are shown. This development can be considered as a significant improvement in the field of quantum radiometry, since, due to the pulsed operation and sub-Poisson statistics of the light source, any count rate saturation effects of the single-photon detector are diminished, see Figure 5, where the calibration results for using single-photon sources are compared with the results obtained when using an attenuated laser. The measurement uncertainty budget for the calibration of a Si-SPAD detector against a low-noise analogue reference detector by using a single-photon source based on a single quantum dot at 930 nm is shown in Table 1.

Table 1: Measurement uncertainty budget for the calibration of a Si-SPAD detector against a low-noise analogue reference detector by using a single-photon source based on a single quantum dot at 930 nm [6].

Source of uncertainty	Value	Standard uncertainty (%)	Contribution (%)
Planck constant $h$	$6.62607015 \times 10^{-34} \text{ J}\cdot\text{s}$	0	0
Speed of light $c$	$299792458 \text{ m}\cdot\text{s}^{-1}$	0	0
Wavelength $\lambda$	929.8 nm	0.01	0.01
Spectral responsivity $s$	$0.5886 \times 10^{12} \text{ V}\cdot\text{W}^{-1}$	0.53	17.97
After-pulsing probability $p_a$	0.0208	4.81	0.68
Connect / disconnect fibre factor $f_{\text{conn}}$	1	0.50	16.19
Count rate $M_{\text{total}}$	$825500 \text{ s}^{-1}$	0.08	0.39
Dark count rate $N_{\text{dark}}$	$231 \text{ s}^{-1}$	1.02	0.002
Temporal stability $f_{\text{temp}}$	1	0.99	63.73
Voltage $U$	0.3082 V	0.13	1.03
<b>Combined uncertainty <math>u_c</math></b>		<b>1.24</b>	<b>100</b>

<sup>6</sup> H. Georgieva et al., “Absolute calibration of a single-photon avalanche detector using a bright triggered single-photon source based on an InGaAs quantum dot”, Opt. Express 29, 23500 (2021)

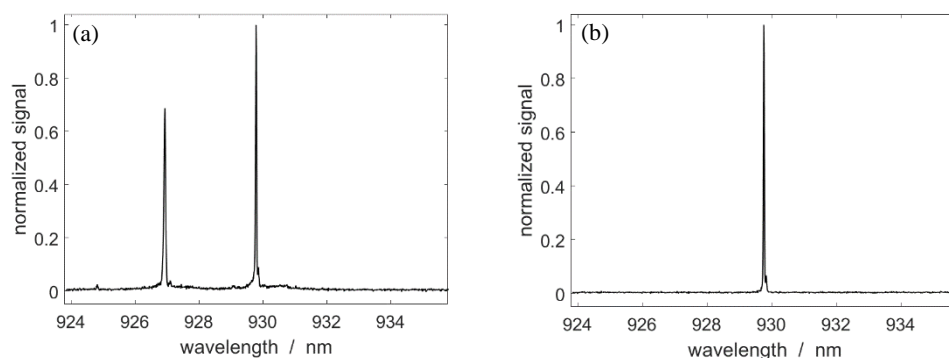


Figure 4. (a) Spectrum of the selected QD. (b) Spectrally filtered QD emission with an emission wavelength of  $\lambda = (929.8 \pm 0.1)$  nm.

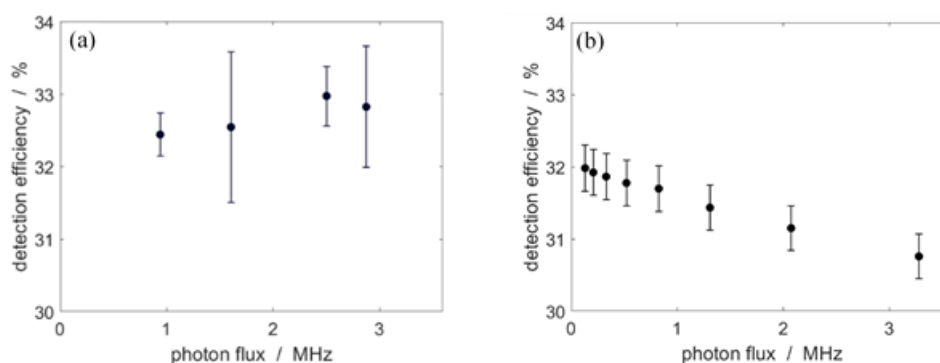


Figure 5. Si-SPAD detector calibration. (a) Calibration using the spectrally filtered QD emission for a direct comparison with an analogue reference detector. (b) Calibration using a strongly attenuated laser source, where the incoming photon flux has been indirectly determined from a calibration of two variable attenuators. The error bars in (a) and (b) indicate the standard measurement uncertainty.

The results obtained for the infrared single-photon source operated at 1550 nm and characterised by USTUTT and NPL, see sections 4.2.3.3 and 4.4.4.3.

#### 4.1.3 Single-photon sources based on molecules

Organic dye molecules are bright single photon sources which can be produced massively with nominally identical properties at low cost. They can be operated both at room and cryogenic temperature; in the latter case (below 4K) their quantum yield moves close to unity, and their emission in the 00-zero phonon line becomes pronounced (branching ratio  $\sim 0.3$ - $0.5$  of the total emission) and Fourier-limited, i.e., they are able to provide highly indistinguishable photons. To operate molecules as single photon sources, CNR has developed a simple procedure that is able to provide hundreds of useful emitters in a single sample. It consists of the dispersion of nanocrystals of anthracene doped with DBT [7] over a gold mirror. With a sufficiently low density of the fluorophore, most of the nanocrystals contains zero or one emitter, and thanks to their average dimensions, this emitter can lay around 100 nm away from the reflecting surface. This condition determines an effective redirection of the emission within a narrow cone around the polar axis, enhancing the collection efficiency even in case of limited numerical aperture [8]. Such a configuration simplifies the search for good SPSs, since the bright spots that can be seen in a fluorescence map are very likely to correspond to individual emitters under optimal conditions. The SPS can also be operated at room temperature, with a similar performance except for spectral width (around 50 nm) and no indistinguishability. However, optimal emission properties are obtained with a cryogenic environment at 3 K. CNR has verified in [9] that emission properties are kept for operation up to 10K, except for indistinguishability. The SPS does not require resonant pumping and a cross-polarisation setup in detection. High purity and indistinguishability is reported also under pulsed

<sup>7</sup> S. Pazzagli et al., ACS Nano 12 (5), 2018

<sup>8</sup> S. Checcucci et al., Light:S&A 6, 2017

<sup>9</sup> P. Lombardi et al., Adv. Quantum Technol. 3 (2), 2020

non-resonant excitation [10]. The minimal setup to operate the SPS consists of a simple epi-fluorescence microscope, see Figure 6. One of the DBT:Ac samples was used for the calibration of single-photon detectors. Lombardi et al [9] performed for the first time a direct calibration of a Si-SPAD detector using a continuously operated single-photon source. The source used for this experiment had a photon flux at the location of the detector of up to  $1.32 \times 10^6$  photons per second, a value for  $g^{(2)}(0)$  (indicating the single-photon purity)  $< 0.1$  and a spectral bandwidth of  $< 0.2$  nm. This optical radiant flux can still be reasonably measured with conventional silicon photodiodes, see e.g. [11]. Figure 7 summarises in an artistic manner the properties of the DBT:Ac single-photon source.

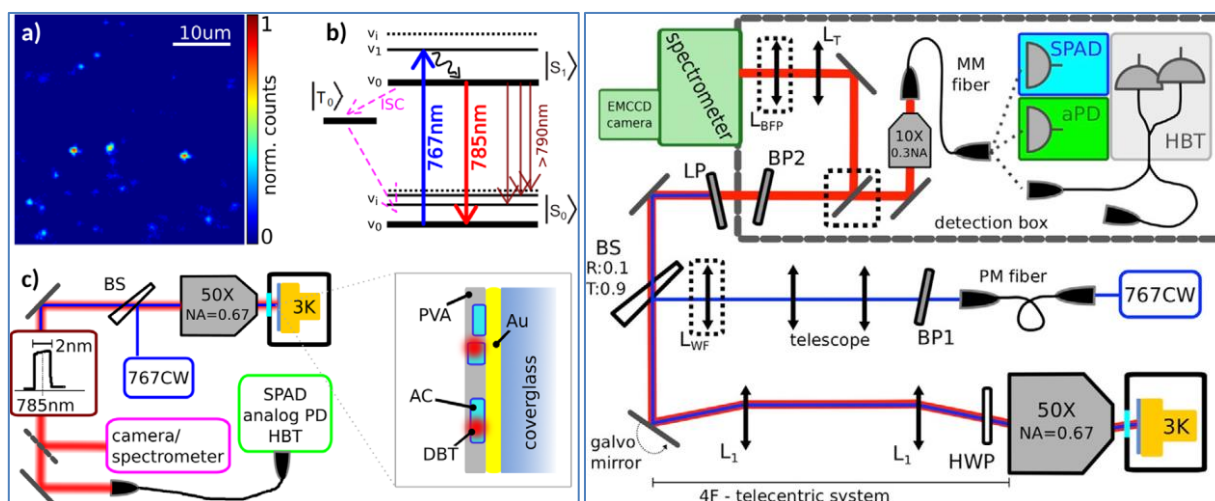


Figure 6. Left: a) Wide-field (WF) fluorescence image: zoom ( $40 \mu\text{m}^2 \times 40 \mu\text{m}^2$ ) on a region of the sample showing bright nanocrystals. b) Blue-detuned (767 nm) pumping scheme used to collect photons emitted into the 00-ZPL (785 nm). In order to properly model the molecule photo-physics, the metastable triplet state should be taken into account. Fluorescence is inhibited when the molecule is in its triplet state, which is hence responsible for blinking. However, this state is very unlikely populated in the case of DBT in Ac, with a probability (namely inter system crossing yield) ISC  $< 10^{-5}$ . c) Simplified sketch of the optical setup used for the measurement reported in the paper and sketch of the device operated as a single-photon source. Au, gold; AC, anthracene; DBT, dibenzoterrylene; PVA, polyvinyl alcohol. Right: detailed sketch of the optical setup: dashed squares mark flipable elements, PM, polarisation maintaining fibre, BP, bandpass filter, LWF, lens for wide-field imaging, BS, beam sampler, L1, lenses for telecentric system, HWP, half wave plate, LP, long-pass filter, LT, tube lens, LBFP, lens for back focal plane imaging, MM, multi-mode fibre, SPAD, single photon counting module, aPD, analogue Si photodiode, HBT, fibre-based Hanbury-Brown and Twiss interferometer.

The calibration process (for details see [9]), is in this case rather simple, i.e., the substitution method is used. The photon flux from the single-photon source was alternatively measured with the SPAD detector and with an analogue reference Si detector, which is traceable to the standard for optical radiant flux, i.e., the cryogenic radiometer. Both detectors were equipped with an FC/PC multimode fibre port, so that the output from the fibre coupled single-photon source can be easily measured. The SPAD detection efficiency  $\eta_{\text{SPAD}}$  can then be calculated from  $\eta_{\text{SPAD}} = \frac{N_{\text{SPAD}}}{N_{\text{Ref}}} = \frac{N_{\text{SPAD}}}{\phi_s E} = \frac{N_{\text{SPAD}}}{I_f / s_{\text{ref}} E}$ , where  $N_{\text{SPAD}}$  is the count rate measured with the SPAD

detector,  $N_{\text{ref}}$  is the photon flux, determined with the reference detector via the measurement of the photocurrent  $I_f$ , using the known spectral responsivity  $s_{\text{ref}}$  and the photon energy  $E (= 2.53 \times 10^{-19} \text{ J})$  for a photon at 785.6 nm). In Figure 7,  $\eta_{\text{SPAD}}$ , determined as described above, for the SPAD detector is depicted for photon rates between  $0.144 \times 10^6$  and  $1.32 \times 10^6$  photons/s, corresponding to a power range between 36.5 fW and 334 fW. It can be seen from the figure that the photon rate approaches the regime where the detector

<sup>10</sup> P. Lombardi et al., Appl. Phys. Lett. 118 (20), 2021

<sup>11</sup> G. Porrovecchio, M. Šmid, M. López, H. Hofer, B. Rodiek, S. Kück, “Comparison at the sub-100-fW optical power level between a high sensitive, low noise Silicon photodiode and a low optical flux measurement facility based on a double attenuator technique”, Metrologia 53 1115–1122, (2016), doi:10.1088/0026-1394/53/4/1115.

dead time affects the detection efficiency measurement  $\eta_{\text{SPAD}}$  [12]. In this respect, a considerable improvement for the calibration process would be an operation of the single-photon source in pulsed mode while maintaining the high photon flux. The standard uncertainty varies in the range of 2 % to 6 %, depending on the photon rate, i.e., the lower the photon rate, the higher the uncertainty. It was calculated according to the Guide to the Expression of Uncertainty in Measurement (GUM) [13]. The highest contribution is the statistical noise of the reference detector, which contributes to more than 90 % of the overall uncertainty.

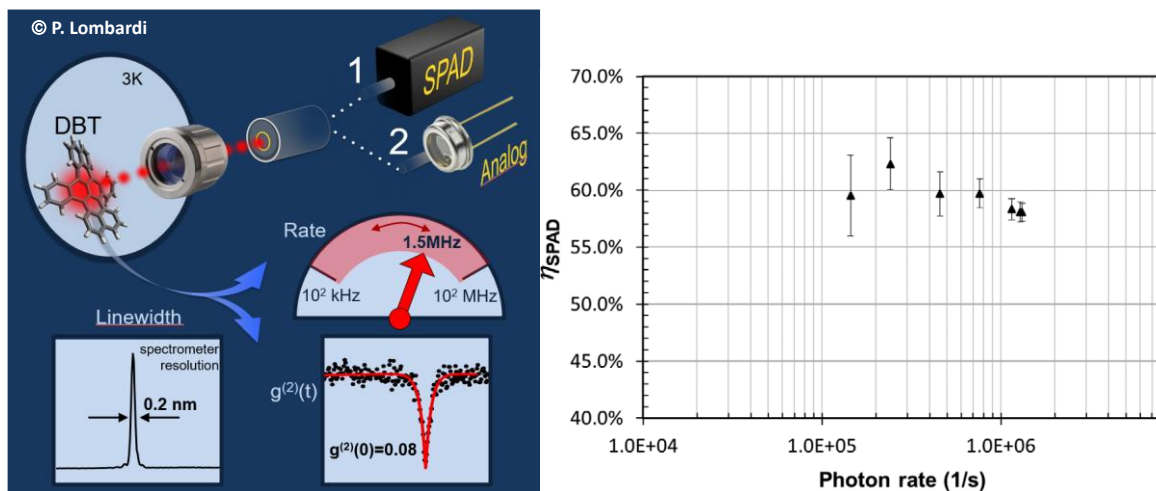


Figure 7. Left) Artistic summary of the properties of the DBT:Ac single-photon source used for the calibration of the Si:SPAD detector. © P. Lombardi. [9] Right) Calibration result for the SPAD detection efficiency (Perkin Elmer, SPCM-AQRH-13-FC) using the molecule-based single-photon source and a low-noise reference analogue detector [9].

#### 4.1.4 Summary

Although the objective 1, i.e., the realisation of a single-photon source exhibiting *simultaneously* the parameters for a photon rate  $> 1 \times 10^6$  photons per second, an emission bandwidth  $< 2$  nm and a high purity emission indicated by a  $g^{(2)}(\tau = 0)$  value  $< 0.05$ , was not achieved, the sources developed within this project allowed the absolute calibration of single-photon detectors against analogue detectors and are therefore a significant step forward towards the routine use of single-photon sources in National Metrology Institutes. Table 2 summarises the results obtained within this project.

Table 2. Summary of obtained results with single-photon sources applied for SPAD detection efficiency calibration.  $N_{\text{ph}}$ : total photon flux,  $Dl$ : spectral bandwidth (FWHM),  $N_{\text{ph},i}(l)$ : maximum spectral photon flux (normalised to a radiometric relevant bandwidth of 1 nm),  $g^{(2)}(\tau = 0)$ : value of the second order correlation function at  $\tau = 0$  (indicator of single-photon purity),  $T$ : operation temperature,  $u(h)$ : uncertainty realised in SPAD detection efficiency calibrations.

Type of source	Impurity centre in (nano-) diamond	Single molecule	Semiconductor quantum dot
Emitter	NV	DBT:Ac	InGaAs
$N_{\text{ph}}$ (photons/s)	$2.6 \times 10^5$	$1.32 \times 10^6$	$2.55 \times 10^6$
$Dl$ (nm)	$\gg 100$	$< 0.2$ nm	$< 42$ pm
$N_{\text{ph},i}(l)$ (photons/(nm s))	$\gg 1$ 100 (@ $\gg 685$ nm)	$1.32 \times 10^6$ (@ 785.6 nm)	$2.55 \times 10^6$ (@ 929.8 nm)
$g^{(2)}(\tau = 0)$	0.23	0.08	0.24
$T$ (K)	Room temperature	3	10
$u(h)$	- (not carried out yet)	2 % ... 6 % (CW)	0.9 % ... 3.2 % (pulsed)

<sup>12</sup> M. López, H. Hofer, S. Kück, "Detection efficiency calibration of single-photon silicon avalanche photodiodes traceable using double attenuator technique, *Journal of Modern Optics* 62, S21 – S27 (2015), <http://dx.doi.org/10.1080/09500340.2015.1021724>.

<sup>13</sup> Guide to the Expression of Uncertainty in Measurement, 1st ed., BIPM, September 2008.

## 4.2 Objective 2

*To assess new materials and concepts for single-photon sources, such as 2D materials and coupling designs to optimise the collection efficiency. To assess the impact of excitation schemes on the quantum optical properties of single-photon sources.*

### 4.2.1 2D materials based on hexagonal boron nitride and transition metal dichalcogenides

Recent years have seen an increased interest in defects in two-dimensional (2D) materials and the study of their single-photon emission properties [14, 15, 16, 17, 18, 19, 20, 21, 22, 23, 24]. 2D materials refer to one-atom thick layers which can be synthesised by chemical vapour deposition (CVD) methods, or isolated from bulk layered crystals, such as hexagonal boron nitride (hBN) and transition-metal dichalcogenides (TMDCs). The aim of this work within the SIQUST project was to study naturally occurring, or artificially created, using focused ion beam (FIB), single-photon emitters in hBN and TMDCs. single-photon characteristics of naturally occurring defects in 2D materials were investigated, which were either prepared in-house by mechanical exfoliation, or obtained from commercial sources and collaborators. The work involved scanning probe microscopy (SPM) and optical spectroscopy characterisation of mechanically exfoliated hBN (monolayers and multilayers), TMDCs (monolayers and bilayers of MoS<sub>2</sub> and WSe<sub>2</sub>) and CVD monolayer hBN. SPM was applied to probe the structural characteristics of the 2D materials investigated in this study. Photoluminescence (PL) spectroscopy was used to identify candidate defects for assessment of their single-photon nature by Hanbury Brown and Twiss (HBT) interference. Furthermore, the work involved artificial creation of defects in mechanically exfoliated hBN material by using FIB milling. Irradiated arrays of defects produced using Ga<sup>+</sup> ions were investigated using SPM and PL spectroscopy to assess the structural, electronic and optical nature of the defects.

#### Summary

Native and FIB created defects in 2D materials were characterised by scanning probe microscopy for their structural characteristics at NPL and PTB. PL spectroscopy was used to identify emitting defects in monolayer, bilayer and multilayers of hBN and TMDCs, and HBT interferometry to further assess the anti-bunching properties of the emission. The sample material and associated observations of SPE characteristics for each material investigated are summarised in Table 3.

<sup>14</sup> Koperski, M. et al. Single photon emitters in exfoliated WSe<sub>2</sub> structures. *Nat. Nanotechnol.* 10, 503–506 (2015).

<sup>15</sup> Tran, T. T., Bray, K., Ford, M. J., Toth, M. & Aharonovich, I. Quantum emission from hexagonal boron nitride monolayers. *Nat. Nanotechnol.* 11, 37–41 (2015).

<sup>16</sup> Tonndorf, P. et al. Single-photon emission from localized excitons in an atomically thin semiconductor. *Optica* 2, 347 (2015).

<sup>17</sup> Kumar, S., Kaczmarczyk, A. & Gerardot, B. D. Strain-Induced Spatial and Spectral Isolation of Quantum Emitters in Mono- and Bilayer WSe<sub>2</sub>. *Nano Lett.* 15, 7567–7573 (2015).

<sup>18</sup> Chakraborty, C., Kinnischtzke, L., Goodfellow, K. M., Beams, R. & Vamivakas, A. N. Voltage-controlled quantum light from an atomically thin semiconductor. *Nat. Nanotechnol.* 10, 507–511 (2015).

<sup>19</sup> He, Y.-M. et al. Cascaded emission of single photons from the biexciton in monolayered WSe<sub>2</sub>. *Nat. Commun.* 7, 13409 (2016).

<sup>20</sup> Palacios-Berraquero, C. et al. Atomically thin quantum light-emitting diodes. *Nat. Commun.* 7, 12978 (2016).

<sup>21</sup> Jungwirth, N. R. et al. Temperature Dependence of Wavelength Selectable Zero-Phonon Emission from Single Defects in Hexagonal Boron Nitride. *Nano Lett.* 16, 6052–6057 (2016).

<sup>22</sup> Martínez, L. J. et al. Efficient single photon emission from a high-purity hexagonal boron nitride crystal. *Phys. Rev. B* 94, 121405 (2016).

<sup>23</sup> Choi, S. et al. Engineering and Localization of Quantum Emitters in Large Hexagonal Boron Nitride Layers. *ACS Appl. Mater. Interfaces* 8, 29642–29648 (2016).

<sup>24</sup> Chejanovsky, N. et al. Structural Attributes and Photodynamics of Visible Spectrum Quantum Emitters in Hexagonal Boron Nitride. *Nano Lett.* 16, 7037–7045 (2016)

Table 3: Summary of 2D materials investigated for single photon emission from native defects.

Sample material	Sample number	Single-photon emission	Number of SP emitters found	Notes
Exfoliated monolayer hBN	over 20 flakes	No	0	Emitters too unstable for HBT measurements.
Exfoliated multilayer hBN	over 100 flakes	Yes	> 50	All emitters in large flakes. Varying stability.
CVD monolayer hBN	2 (many regions)	Yes	> 20	Extensive searching required. Unstable.
Exfoliated monolayer and multilayer MoS <sub>2</sub>	1 (several regions)	No	0	Direct-Indirect transition of bandgap observed when going from monolayer to multilayer. No single photon emission.
Bilayer MoS <sub>2</sub>	1	No	0	Emission dominated by polymer residue.
Bilayer WSe <sub>2</sub>	1	No	0	No strong emission.

No single-photon emitting defects were identified in exfoliated monolayer hBN or the monolayer/bilayer/multilayer TMDCs investigated in this work.

The characterisation of native defects in exfoliated multilayer hBN showed that some of the defects are relatively stable and bright, with good quality single-photon emission. However, varying photostability of the emission is very common, with blinking, bleaching and spectral wandering behaviour observed. Poor emission stability was also found for the native defects of CVD-grown monolayer hBN.

The wide spectral range and poor photostability of the native defects' emission present a significant barrier to the development of single photon sources.

The FIB approach, although successful in creating arrays of artificial defects, resulted in poor emission for the range of parameters investigated in this study.

#### 4.2.2 Coupling designs to optimise the collection efficiency - Single molecules in solid-state matrices

Single molecules in solid-state matrices were proposed as sources of single-photon Fock states 20 years ago due to their outstanding brightness. Specific guest-host systems, such as the one extensively studied at CNR (i.e., dibenzoterrylene in anthracene, DBT:AC) appear well-suited for integration in hybrid photonic circuits due to: a high emission branching ratio in the transition of interest; a low refractive index of the host matrix; the possibility of having high-quality emission when embedded in sub-micrometric particles [25]. The challenge to date for integrating molecule-based single-photon sources (SPSs) in photonic chips has been the development of fabrication procedures which maintain the high crystallinity of the host matrix, which is required to guarantee the optical properties of the emitters.

Integration in waveguides: Strategies based on three fundamental components have been explored, these are molecule-based SPS in the form of a nanocrystal (NC) suspension in water; direct laser writing (DLW) to fabricate polymeric structures; semiconductor chips with dielectric photonic structures. As preliminary steps, CNR has demonstrated the substantial compatibility of our nanocrystals with the resists used for DLW

<sup>25</sup> S. Pazzagli et al., "Self-Assembled Nanocrystals of Polycyclic Aromatic Hydrocarbons Show Photostable Single-Photon Emission", ACS Nano 12 (5), 4295-4303 (2018)

lithography and polyvinyl alcohol (PVA); a technique for the localised deposition of few NCs based on a micro-infiltration setup that is able to deliver a micro-droplet of suspension in predetermined places.

Geometries/Strategies: Four different approaches to reach a scalable platform in which SPSs are efficiently coupled to guided modes were explored. The original plan of the project included two alternative approaches:

Approach #1: Mixing NCs with DLW resists, it is possible to fabricate a polymeric structure around preselected molecules. As a first step, the case of NCs buried in simple waveguides (WGs) was investigated. Due to the proximity of the refractive indices of polymeric resists and glass, the WGs have to be suspended over the substrate in order to hold a strong confinement of the field, as required for high SPS-WG coupling. An arch-like WG with a bending radius of 6  $\mu\text{m}$  was designed, with direct coupling to far-field through the glass substrate. Figure 8 shows a typical device imaged using scanning electron microscopy (SEM).

Approach #2. A pre-fabricated ridge WG in  $\text{Si}_3\text{N}_4$  on  $\text{SiO}_2$  with a hole at the centre, terminated with a grating coupler for far-field coupling, was also investigated (Figure 9). Such a configuration enables the positioning of an NC inside the hole, close to the guided mode field maximum. According to finite-difference time-domain (FDTD) simulations, an enhancement of the coupling efficiency with respect to the case of NC next to a simple ridge WG by a factor 2 is expected. Localised delivery of a few NCs was obtained with the help of a micro-infiltration instrument (Eppendorf FemtoJet). The selected NC was then protected by a PVA pad fabricated via DLW, while the other nanocrystals are washed out.

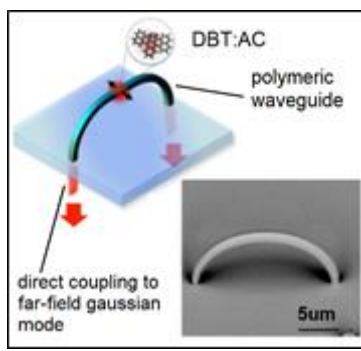


Figure 8. Polymeric fabricated structure.

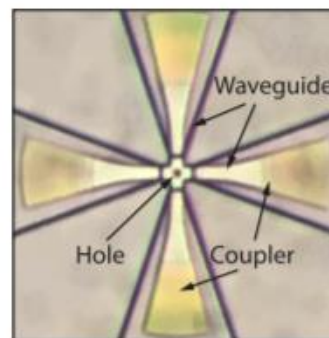


Figure 9. SiN ridge WG with hole.

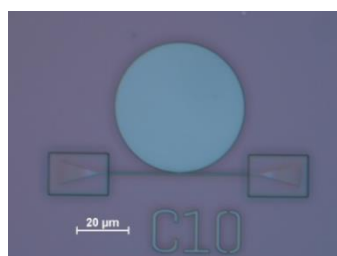


Figure 10.  $\text{Si}_3\text{N}_4$  disk resonators.

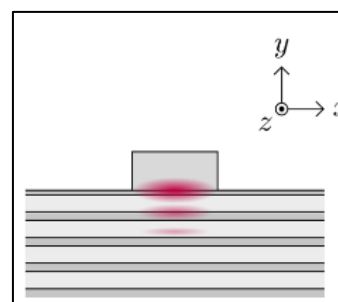


Figure 11. Polymeric BSW WGs.

In the second part of the project two other solutions were explored, inspired by the preliminary results with approaches #1 and #2:

Approach #3. Starting from the expertise accumulated working on strategy #2, pre-fabricated dielectric disk resonators were considered, coupled to the far-field with the well-established CNR WG+grating coupler design (Figure 10). On one hand, this geometry is more suitable for successful delivery of few NCs in the useful region by micro-infiltration; on the other, the side the photonic resonances can be exploited to enhance both the emission properties of the molecules and the coupling to the WG mode through the Purcell effect. Disks of 50  $\mu\text{m}$  diameter, which provide a free spectral range, in the order of 2 nm, were assessed.

Approach #4. As a follow-up to strategy #1, in order to overcome the constraints given by suspended geometries, polymeric ridge WGs fabricated on top of a dielectric Bragg reflector (DBR), were considered (Figure 11). In this configuration one can take advantage of the presence of guided modes trapped in the air-dielectric interface, similar to surface plasmon polaritons on metallic surfaces, named Bloch surface waves (BSW). These modes can be conveniently conveyed and spatially localised by shaping an additional layer on top of the multi-layer. With this protocol it is expected to fabricate WGs with propagation losses as low as  $\sim 10^4$  dB/cm [26].

Measurements: For each approach the optical characterisation of the simple photonic part was first performed. In order to enable a quantitative analysis of signals coming from the guided mode, the couplers' far-field efficiency and the input mode matching from free space have to be evaluated.

#### Summary

Table 4 summarises the results of the investigations into optimising the coupling of single-photon emission from single-molecules into waveguides. Measurements of photon purity, i.e.  $g^{(2)}(0)$ , and indistinguishability for nanocrystals embedded in waveguides were not achievable within the project, but measurements performed on a system comprising a nanocrystal on top of a gold mirror on which a solid immersion lens was fabricated around the nanocrystal, yielded  $g^{(2)}(0) = 0.00 \pm 0.03$  and indistinguishability  $\sim 0.8$ .

Table 4: Coupling efficiencies for various waveguide structures.

	<b>Polymeric waveguide</b>	<b>Si<sub>3</sub>N<sub>4</sub> on SiO<sub>2</sub> ridge waveguide</b>	<b>Si<sub>3</sub>N<sub>4</sub> disk resonator</b>	<b>Polymeric ridge waveguide on top of Bragg mirror</b>
<b>Emitter-waveguide coupling efficiency</b>	~ 10 %	~ 10 %	~ 78 %	Not yet measured
<b>Comment</b>	Estimated from measurement data	Estimated from measurement data	Predicted from limited experimental data	Device designed within SIQUST

#### 4.2.3 Coupling schemes for quantum dots and the impact of excitation schemes on the quantum optical properties of single-photon sources

Several outstanding results have been achieved by QD-based single-photon sources with high photon extraction efficiency in combination with almost ideal single-photon purity. In order to reach these goals, efforts have been made to develop advanced deterministic nanofabrication platforms and to optimise the optical pumping scheme from the simple non-resonant mechanism to the more challenging and currently more effective resonant excitation.

##### 4.2.3.1 NIR (930 nm region) optically-pumped devices

Four different excitation schemes and their impact on the suppression of multi-photon events and the degree of indistinguishability of subsequently emitted photons were investigated for InGaAs/GaAs quantum dots emitting in the near infrared around 930 nm. Amongst them are non-resonant, quasi-resonant, resonant, and two-photon resonant excitation. Additionally, the effect of temporal separation between excitation pulses was evaluated.

##### Non-resonant excitation:

This kind of excitation generates free charge carriers in the bulk material (GaAs) for above bandgap excitation and/or in the InGaAs wetting layer that thermalise into the QDs. This excitation scheme is most easy to realise but there is a high probability that a QD might capture another e-h pair after its initial recombination process and the large amount of free charge carriers leads to dephasing and slight energy shift of excitonic states in QDs via Coulomb interaction. The consequence is an increased probability of multi-photon emission events even under pulsed excitation and the visibility of indistinguishable photons is reduced, too. The latter effect can be reduced by choosing a smaller temporal distance between excitation pulses (e.g., 2 - 4 ns) and by increasing the spontaneous emission rate via light-matter interaction in, e.g., a microcavity by exploiting the Purcell effect. This positive effect of the Purcell effect on the indistinguishability of consecutively emitted photons holds true for the following excitation schemes as well.

<sup>26</sup> T. Perani and M. Liscidini, "Long-range Bloch surface waves in photonic crystal ridges", *Optics Lett.* 45 (23), 6534 (2020)

### Quasi-resonant excitation

Here, the QD is populated with charge carriers via excitation into a higher QD state or by phonon-aided processes. Consequently, there are almost no free charge carriers in its surrounding (at low temperatures) and the diminishing effects from section (2.1.1) are drastically reduced. This is evident from Figure 12(a) where the FWHM of a trio's emission line under pulsed p-shell excitation is as small as  $62 \mu\text{eV}$ . The corresponding  $g^{(2)}(0)$  value for this example equals  $(12 \pm 2)\%$  (Figure 12(b)).

### Resonant excitation:

Resonant excitation takes place via direct population of the QD's ground state via a resonant light/laser source. However, the resonant photons from the exciting laser overlap spectrally with the QD's emission and highly effective stray-light suppression techniques have to be employed to damp the stray light from the excitation source by at least six orders of magnitude. The direct population of the ground state requires no energy relaxation as in the case of p-shell excitation and the quantum optical properties of the emission events are further improved. This is reflected in Figure 12(c) by a decreased FWHM as compared to Figure 12(a) down to a value of  $51 \mu\text{eV}$  and in Figure 12(d) by a  $g^{(2)}(0)$  value of  $(7.3 \pm 0.5)\%$ . It must be noted that the present  $g^{(2)}(0)$  values are not the best ones and can be easily surpassed by non-resonant experiments on high-quality emitters, but the general trend of enhancing the emission properties and quantum nature of emission by more resonant excitation is clearly demonstrated for one and the same QD. The same holds for the generation of indistinguishable photons which is shown in Figure 13 for one and the same QD.

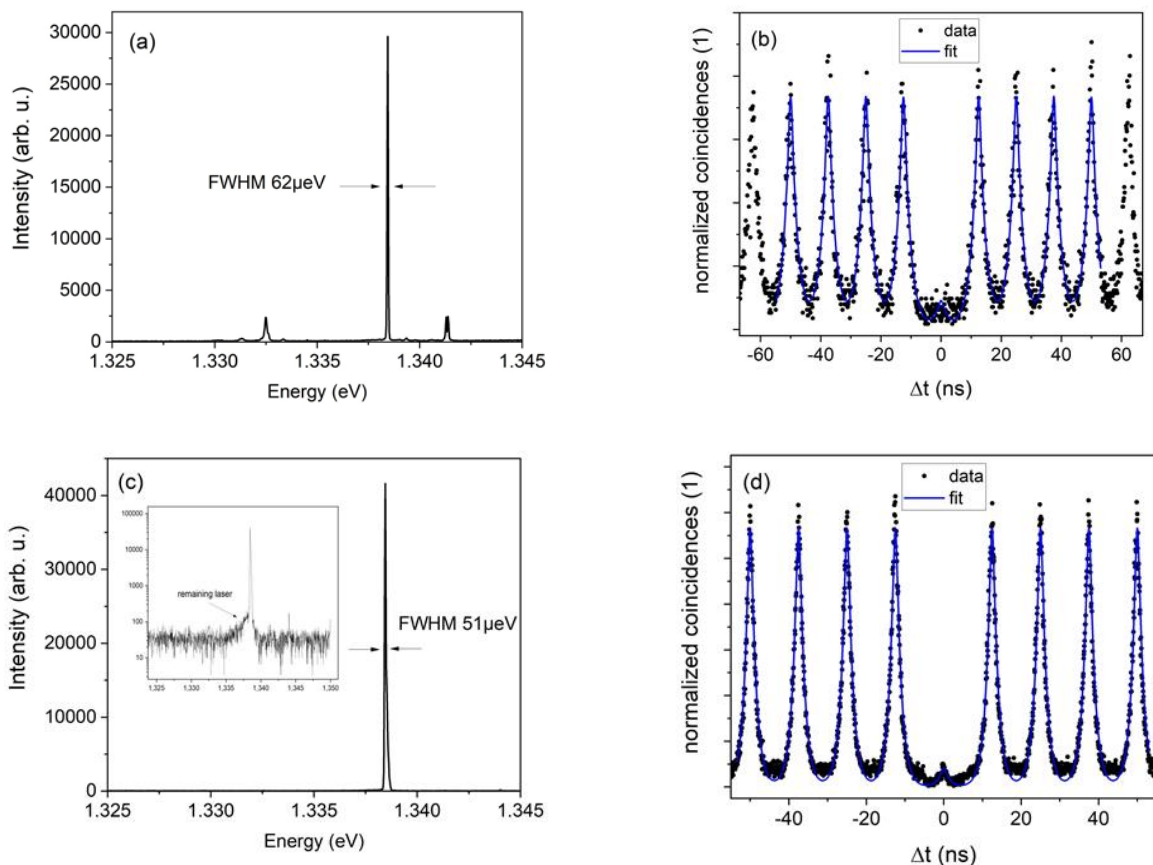


Figure 12. (a) Spectrum of an InGaAs/GaAs QD under pulsed (2 ps length) p-shell excitation in saturation of a trion state at an excitation power of  $5 \mu\text{W}$ . (b) Second order photon autocorrelation measurement (black dots) on the line in (a) and corresponding deconvoluted fit (blue solid line) revealing an antibunching value of  $g^{(2)}(0)_{\text{fit,p-shell}} = (12 \pm 2)\%$ . (c) Spectrum under pulsed resonant excitation, the inset shows the same data in logarithmic intensity-scaling to make visible the remaining scattered laser. (d) Second order photon autocorrelation measurement on the line in (c) and corresponding fit yielding  $g^{(2)}(0)_{\text{fit,s shell}} = (7.3 \pm 0.5)\%$ .

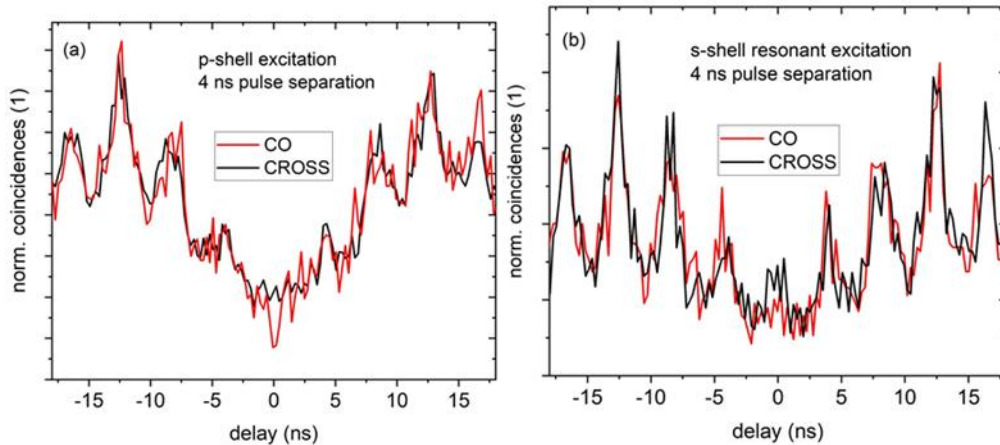


Figure 13. HOM measurements under pulsed excitation with a pulse separation of 4 ns for p-shell excitation (a) and s-shell resonant excitation (b). Although the statistics are rather poor, the positive effect of resonant excitation is obvious around zero-time delay.

Two-photon resonant excitation:

This kind of excitation is possible only for, e.g., the biexciton state, as momentum conservation requires the generation of, e.g., two excitons. Nevertheless, here it is very efficient and thanks to the biexciton binding energy, the laser energy is shifted with respect to the biexciton and exciton emission energies (Figure 14) and can easily be filtered out. TUB was able to demonstrate a biexciton-exciton polarisation entanglement of 80 % [27]. This kind of resonant excitation also allows for autocorrelation measurements that are not diminished by the laser’s stray light. This is demonstrated in Figure 15 by a CW autocorrelation trace for an excitonic transition under two-photon resonant excitation.

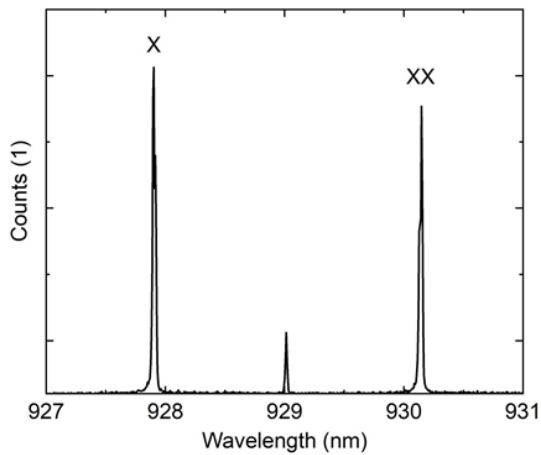


Figure 14. Demonstration of the population of the biexciton state via two-photon resonant excitation with emission from the biexciton and exciton. Thanks to the biexciton binding energy, the laser energy is shifted with respect to exciton and biexciton emission.

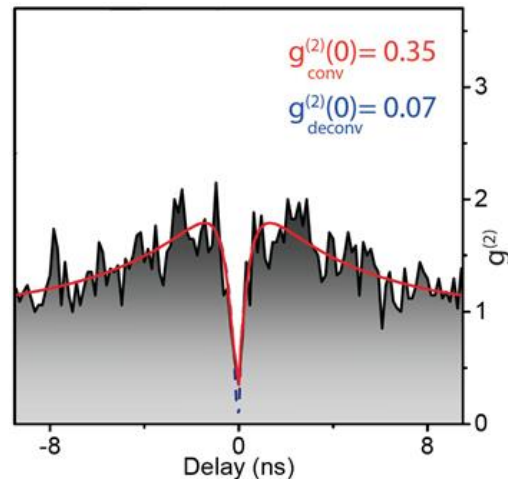


Figure 15. Autocorrelation measurement for an excitonic transition under cw two-photon excitation. Bunching on a longer time scale can be attributed to blinking of the emitter. The deconvoluted  $g^{(2)}(0)$  value amounted to 0.07.

4.2.3.2 NIR (935 nm region) electrically-driven devices

From the point of view of the excitation, most of the reported SPSs rely on optical excitation, as the number of electrically driven sources are scarcer. Since the seminal experimental realisation of such a quantum light

<sup>27</sup> S. Bounouar et al., “Generation of maximally entangled states and coherent control in quantum dot microlenses”, Appl. Phys. Lett. 112, 153107 (2018)

emitting diode [28], different groups have achieved high operation rates. Direct injection in a p-n diode structure was indeed very promising although it also presented two main limitations: firstly, it is difficult to get independent control of the single-photon rate and wavelength since both depend on the current flowing through the diode; secondly, direct current driving of the quantum emitter is inefficient when the current must flow through a nanopatterned structure, as required in a nanophotonic environment.

Within SIQUEST, the CSIC explored how to overcome these difficulties by using hybrid electro-optical pumping schemes in a monolithic device. The resulting device design has been patent protected during the project and comprises two light-emitting diodes (LEDs) fabricated back-to-back in a single epitaxial step [29]. At the bottom of the device, the master LED is forward biased and emits classical electroluminescence towards the slave LED sitting on top. InGaAs quantum dots (QD) embedded in the slave LED absorb this classical light and emit quantum light (single photons). Tunability can be achieved via the Stark effect by applying a DC voltage at the contacts of the slave LED [30, 31, 32]. Several epitaxial and device layout designs have been fabricated and characterised resulting in two fully functional prototypes.

In addition, single photon extraction optimisation has been explored by designing a novel nanophotonic structure adapted to our excitation scheme which confines most of the QD emission in a narrow cone of  $NA = 0.17$  while reducing the QD emission lifetime by the Purcell effect.

All devices fabricated so far are based on AlGaAs/GaAs heterostructures containing GaAs Quantum Wells (QW) as the pumping material and InGaAs QD to produce single photons around 935 nm.



Figure 16.  $30\ \mu\text{m} \times 30\ \mu\text{m}$  confocal microscopy images of device measured at 4 K.

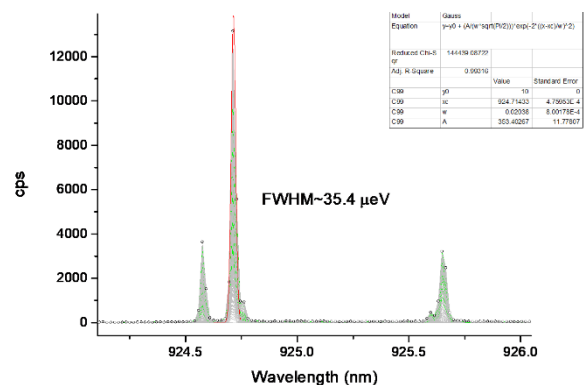


Figure 17. Observed exciton spectrum.

Selected devices were investigated at 4 K using a confocal imaging microscope and high-resolution spectrometers. Once the optimal conditions were set, the single photon purity and first lens rate were determined with SPAD modules in a HBT interferometry setup. By the end of the project, an attempt was made at TUB, to characterise the indistinguishability of the single photon source by HOM interferometry. The single-photon count rate on the measured devices was a factor 10 lower than expected and is currently under investigation. The images in Figure 16 reflect the working principle of the device. On the left panel, the emission at 785 nm results from electroluminescence (EL) generated by  $100\ \mu\text{A}$  injected into the master diode. The blue region delimits the slave diode top mesa. This EL is absorbed and re-emitted as wetting layer luminescence at 870 nm (middle panel) and single QD luminescence at 940 nm (right panel). The InGaAs self-assembled QDs embedded in the slave diode have state-of-the-art properties. In Figure 17, the observed  $\text{FWHM} = 35.4\ \mu\text{eV}$  was limited by the spectrometer resolution. Fine structure splittings around  $40\ \mu\text{eV}$  and

<sup>28</sup> Z. Yuan et al., “Electrically Driven Single-Photon Source”, *Science* 295, 102 (2002)

<sup>29</sup> B. Alén et al “Device for emitting single photons or entangled photon pairs”. European Patent EP 3 361 516 B1 (published 18/12/2019)

<sup>30</sup> B. Alén et al. “Monolithic Quantum Light Source with Hybrid Pumping”, SPIE Optics and Photonics, San Diego - USA 20/08/2018

<sup>31</sup> B. Alén et al. “Development of a plug & play single photon source using electro-optical pumping schemes”, Single Photon Workshop Milán - Italy 21/10/2019

<sup>32</sup> B. Alén et al. “Electrically driven and tunable plug & play single photon sources” Invitada. 3rd International Symposium on Single Photon based Quantum Technologies. Berlin - Germany 15/09/2020

exciton lifetime around 800 ps were typical. 30  $\mu\text{m}$  x 30  $\mu\text{m}$  confocal microscopy images were measured at 4 K. In Figure 18, the emission rate of different exciton complexes from the same QD are shown as a function of the master diode injected current,  $I_{\text{MASTER}}$ . Full saturation is achieved for  $I_{\text{MASTER}} < 70 \mu\text{A}$  corresponding to a first lens single-photon rate of 530 kHz. Below saturation, HBT interferometry was performed revealing a  $g^2(0) < 0.1$ .

Key to our design is the possibility to tune independently the single-photon emission rate and wavelength. This is achieved by varying the master diode current and slave diode voltage, respectively (Figure 19). While the epitaxial structure can still be improved for better functionality, such a crucial result was demonstrated in two different device prototypes (pnp and pn-Schottky).

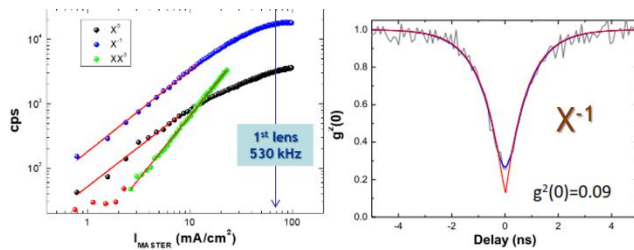


Figure 18. Left: Exciton emission rate vs master current; Right: Single photon purity.

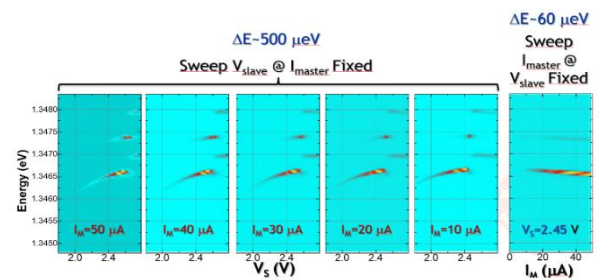


Figure 19. Independent control of emission rate and wavelength.

#### 4.2.3.3 Telecom wavelength (1550 nm region) implementation

The impact of different pumping schemes on the QD properties and on the performance of the emission in the telecom wavelength range has been investigated by USTUTT. The effect on the linewidth, and hence the photon coherence, under different excitation mechanisms, is first discussed. The single-photon emission and photon indistinguishability under CW two-photon excitation, quasi-resonant p-shell pumping and purely resonant excitation is then reported.

As a measure of the coherence, the linewidth of the emission was investigated for excitation of the charge carriers above the band gap of the barrier material (above-band), via the phonon sideband (phonon-assisted) and in resonance fluorescence (RF). In summary, a systematic study on the coherence properties of InAs QDs on a GaAs basis emitting in the telecom C-band has been conducted. Regarding the measurement methods, the limited spectral resolution of a spectrometer can be overcome by employing a Michelson interferometer. This, however, requires sufficient brightness and a longer measurement time. The ability to scan the laser frequency over the QD resonance, while only possible for RF using a precisely tuneable laser, yields reliable information on the linewidth. Another possibility would be to employ a scanning Fabry-Pérot interferometer. Concerning the excitation schemes, switching from above-band to phonon-assisted excitation reduces the FWHM of the emission lines on average from 12.3 GHz to 10.1 GHz, while a resonant excitation yields average values as low as 3.5 GHz, clearly distinguishing it as the most promising for applications requiring a high degree of coherence, such as two-photon interference.

Combining the advantage of resonant state preparation and the possibility of deterministically preparing the radiative decay via the XX-X cascade, two-photon excitation has been identified as an appealing way of excitation, see also [33]. The energy scheme and the corresponding spectrum are shown in Figure 20a; the laser (green) and symmetrically equidistant peaks stemming from the X and XX states (blue and dark red) can be seen. The same integrated intensity of these lines is a first footprint of TPE. The spectral feature, around 1552.5 nm, comes from the scattered laser and from the  $X^+$  state which is pumped via a phonon-assisted process. In Figure 20b an HBT measurement of  $g^{(2)}_{\text{HBT}}(\tau)$  is shown. Superimposed on the expected antibunching feature at zero time-delay, a strong bunching can be seen that has to be taken into account when normalising the data to the Poissonian level (see insets in Figure 20 for long time delays). Taking into account these different effects and the response function of the HBT-system, one yields a value of  $g^{(2)}(\tau) = 0.072 \pm 0.104$ , confirming the high single-photon purity expected for TPE of a QD. The indistinguishability of the emitted XX photons in TPE were also investigated using an unbalanced, fibre-based Mach-Zehnder interferometer. The resulting, maximal post-selected degree of indistinguishability of the photons is calculated to be  $V_{\text{HOM,decon}} = 0.894 \pm 0.109$  ( $V_{\text{HOM,raw}} = 0.713 \pm 0.15$ ) including (excluding) the deconvolution of the data with the system response function. Apart from approaches relying on quantum frequency conversion, this constitutes the first

direct measurement of the mutual, post-selected degree of indistinguishability of QD photons in the telecom C-band, complementing the demonstration of the three basic prerequisites for quantum applications, namely, single-photon emission, entangled-photon pair emission, and indistinguishability.

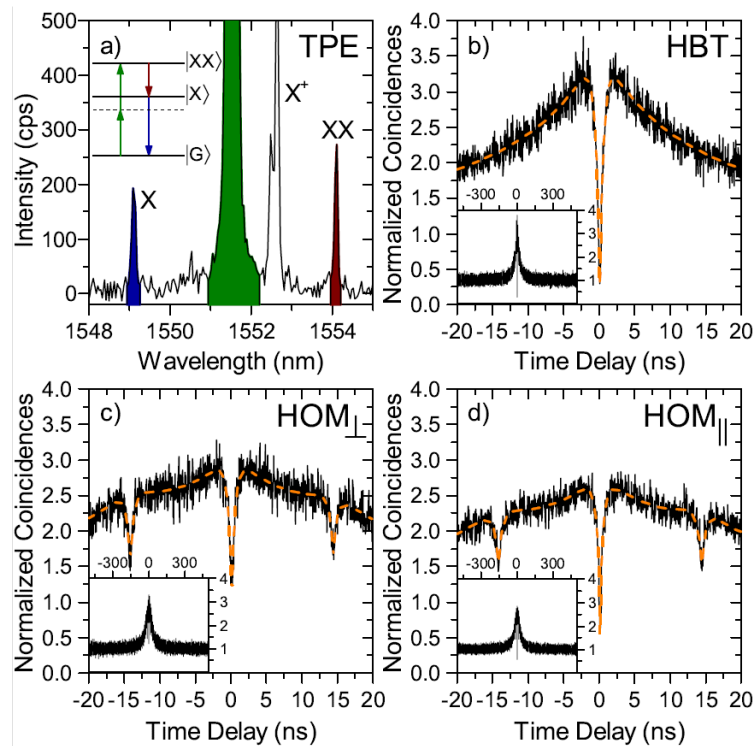


Figure 20. Two-photon excitation: (a) Spectrum and energy diagram. (b) Second order intensity autocorrelation measurement with the fit function (orange). (c) and (d) TPI of distinguishable and indistinguishable photons in TPE with respective fit functions (orange). The insets of (b)–(d) show the same data with a correlation window of  $\pm 500$  ns. The measurements shown in (b)–(d) are performed with a count rate of  $\sim 16$  kcps and an integration time of  $\sim 12$  h. Figure and caption from [33].

Finally, a study on the single-photon purity and indistinguishability under pulsed quasi-resonant p-shell excitation and in pulsed resonance fluorescence of In(Ga)As QDs emitting in the telecom C-band was performed. To evaluate the single-photon purity, the second-order autocorrelation function  $g^{(2)}(\tau)$  is recorded in an HBT setup employing a fibre-based beam splitter. The results along with the respective fit functions are displayed in Figure 21. Note that for the case of p-shell excitation, the measurement artefacts at correlation times other than multiples of the repetition time 20 ns are due to the non-ideal pulse generation, including secondary pulses. To distinguish this from residual multi-photon components at zero time-delay in the correlation measurement, the fit function excludes these artefacts. Both p-shell excitation and RF yield excellent single-photon purity values with  $g^{(2)}(0) = 0.039 \pm 0.006$  and  $g^{(2)}(0) = 0.027 \pm 0.018$ , respectively, including background correction. To evaluate the indistinguishability of consecutively emitted photons in both excitation schemes, an unbalanced Mach-Zehnder interferometer with adjustable polarisation in both arms is employed. The degree of two-photon interference (TPI), i.e. the degree of indistinguishability, is measured by comparing the correlation peak at zero time-delay between intentionally cross-polarised, i.e. perfectly distinguishable, and co-polarised photons. Completely indistinguishable photons impinging in the second beam splitter of the MZI from two different input ports are expected to coalesce and therefore not result in a correlation event detected at zero time-delay. The results are displayed in Figure 22.

<sup>33</sup> C. Nawrath et al., “Coherence and indistinguishability of highly pure single photons from non-resonantly and resonantly excited telecom C-band quantum dots”, Appl. Phys. Lett. 115, 023103 (2019).

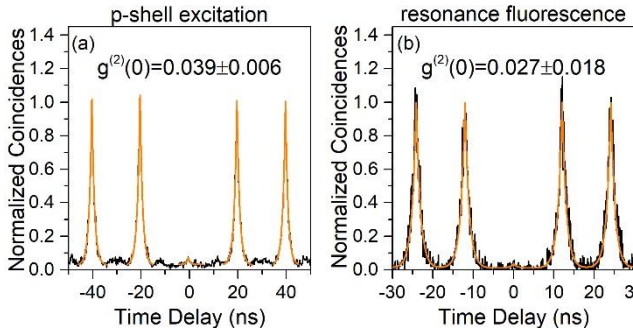


Figure 21. Second-order auto-correlation measurement under (a) pulsed p-shell excitation and (b) in pulsed resonance fluorescence including fit functions (orange).

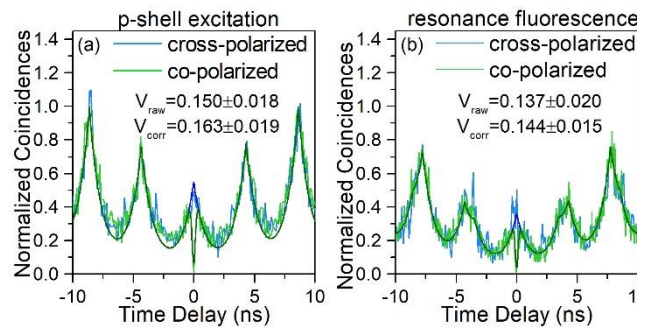


Figure 22. Two-photon interference measurements under (a) pulsed p-shell excitation and (b) in pulsed resonance fluorescence. Measurements and fit functions with cross-polarised photons are displayed in blue, whereas green stands for co-polarised photons.

Note also that in p-shell excitation, the repetition rate of the excitation is set to the delay of the unbalanced MZI of 4.319 ns, whereas in RF the excitation signal is sent into another unbalanced MZI to generate a double-pulse pattern with the respective time separation. For this reason, the correlation histogram for the RF case consists of a series of overlapping peaks. Both data sets are fitted with a model including spectral diffusion and based on the ratio of the areas of the central peak yield TPI visibility values of  $0.163 \pm 0.019$  ( $0.150 \pm 0.018$ ) for p-shell excitation and  $0.144 \pm 0.015$  ( $0.137 \pm 0.020$ ) in RF when correcting for all setup imperfections (only background emission), respectively. These values indicate substantial decoherence mechanisms on the time scale in question for both excitation schemes impacting the degree of indistinguishability. While the identification and mitigation of these processes is of crucial importance to increase the indistinguishability, these measurements represent the first demonstration of the determination of the TPI visibility under pulsed excitation of QDs emitting in the telecom C-band. Furthermore, the pronounced dip in the central peak offers the possibility for time-gated application of these photons. Using such post-selection schemes, a maximal value of  $0.920 \pm 0.0001$  and  $0.955 \pm 0.0001$  for p-shell excitation and RF is attained in this measurement, respectively.

In conclusion, TUB and USTUTT compared p-shell excitation and RF in pulsed mode for QDs emitting directly in the telecom C-band, showing very high single-photon purity values and a proof-of-principle measurement of the degree of indistinguishability for both excitation schemes. An identification and reduction of decoherence mechanisms, is envisioned to transfer the high TPI visibility values measured under post-selection to schemes not relying on such techniques.

#### 4.2.3.4 Summary

Table 5 summarises the measurements obtained for the various excitation schemes studied in the three investigated systems. The monolithic structure, of necessity, could only be pumped at the emission wavelength of the integrated electrical-driven LED. The “standalone” quantum dot structures for 930 nm and 1550 nm emission could be excited at various wavelengths.  $g^{(2)}(0) < 0.1$  was observed in all measurements. Two-photon resonant pumping yielded an entanglement fidelity of 0.8 for the optically pumped 930 nm quantum dots and an indistinguishability  $\sim 0.9$  for the 1550 nm quantum dots.

Table 5: Measured parameters for different quantum dot systems as a function of excitation.

System	Metric	Excitation			
		Non-resonant	Quasi-resonant (12 ± 2) %	Resonant (7.3 ± 0.5) %	Two-photon resonant ~ 7%
930 nm (laser pumped)	$g^{(2)}(0)$				
	Entanglement fidelity				0.8
935 nm (LED pumped)	$g^{(2)}(0)$	< 10%			
1550 nm (laser pumped)	$g^{(2)}(0)$		(3.9 ± 0.6) %	(2.7 ± 1.8) %	(7.2 ± 10.4) %
	Indistinguishability		0.163 ± 0.019	0.144 ± 0.015	0.894 ± 0.109

### 4.3 Objective 3

To establish sources of indistinguishable and entangled photons based on near infrared ( $< 1 \mu\text{m}$ ) QD single-photon sources with a visibility  $> 90\%$  and novel sensing and measurement techniques based on these sources.

Sources capable of generating entangled photon pairs are highly desirable, since most photonic quantum computation [34] and quantum communication protocols [35] rely on their availability. Furthermore, entanglement plays a pivotal role in linking the nodes of quantum networks [36]. In this context, the excitonic-biexcitonic radiative cascade in quantum dots (QDs) has proved to be a very promising candidate for the generation of polarisation entangled photon pairs, in particular because of the triggered emission of photons [37, 38].

This objective dealt with the advantages and limitations of sources of indistinguishable and entangled photons based on near infrared ( $< 1 \mu\text{m}$ ) quantum dot single-photon sources. In particular the work is focused on InGaAs self-assembled semiconductor quantum dots whose yield and performance is enhanced by the integration of a microlens via electron-beam lithography. As characterisation parameters for the purposes of this report,  $g^{(2)}$ , visibility of Hong-Ou-Mandel interference and entanglement fidelity are considered.

#### 4.3.1 Sources of indistinguishable and entangled photons based on near infrared ( $< 1 \mu\text{m}$ ) quantum dot single-photon sources

The controlled generation of photon sources emitting non-classical states of light is a challenging task at the heart of quantum optics, within the SIQUTE project undertaken by TUB for sources  $> 1 \mu\text{m}$ . Aside from the interest in fundamental quantum physics, the related research is strongly driven by applications in photonic quantum technologies, including the fields of quantum communication, quantum computation [39], and quantum metrology [40]. In this context, the realisation of integrated solid-state-based quantum-light sources is of particular interest, due to the prospects for scalability, device integration and applicability [41].

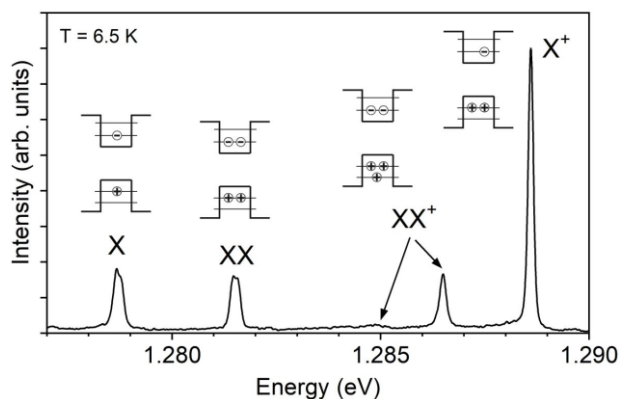


Figure 23: Example spectrum of a single InGaAs/GaAs QD under non-resonant excitation. The different emission lines stem from excitonic complexes (X, XX, X<sup>+</sup>, XX<sup>+</sup>) as sketched close to the respective emission line.

Self-assembled semiconductor quantum dots (QDs) are excellent candidates to realise on-demand quantum light sources [42]. QDs are crystalline clusters of a few hundreds to thousands of atoms embedded in a semiconductor host structure grown by molecular beam epitaxy (MBE) or metal-organic chemical vapour

<sup>34</sup> E. Knill, R. Laflamme, and G.J. Milburn, A scheme for efficient quantum computation with linear optics, *Nature* 9, 46-52 (2001)

<sup>35</sup> W. Tittel and G. Weihs, *Quantum Inf. Comput.* 1, 3-56 (2001)

<sup>36</sup> H. J. Kimble, *Nature* 453, 1023-1030 (2008)

<sup>37</sup> M. Müller, S. Bounouar, K. D. Jons, M. Glassl, and P. Michler, *Nat. Photonics* 8, 224-228 (2014)

<sup>38</sup> S. Bounouar, M. Müller, A. M. Barth, M. Glassl, V. M. Axt, and P. Michler, *Phys. Rev. B* 91, 161302 (2015).

<sup>39</sup> N. Gisin and R. Thew, *Quantum communication*, *Nat. Photonics* 1, 165 (2007)

<sup>40</sup> C. Chunnillall, I. Degiovanni, S. Kück, I. Müller, and A. Sinclair, *Metrology of single-photon sources and detectors: a review*, *Opt. Engineering* 53, 081910 (2014)

<sup>41</sup> S. Rodt and S. Reitzenstein, *Integrated nanophotonics for the development of fully functional quantum circuits based on on-demand single-photon emitters*, *APL Photon.* 6, 010901 (2021)

<sup>42</sup> Y. Arakawa and M. Holmes, *Progress in quantum-dot single photon sources for quantum information technologies: A broad spectrum overview*, *Appl. Phys. Rev.* 7, 021309 (2020)

deposition (MOCVD). The energy band gap of the QD material is chosen to be smaller as compared to the surrounding matrix material, which leads to a three-dimensional confinement potential and discrete energy levels for electrons and holes in the conduction band and valence band, respectively. As a result, QDs feature a discrete emission spectrum including the neutral exciton X, the biexciton XX and charged excitons in case of excess charge carriers (see Figure 23). Pulsed excitation of QDs leads to on-demand emission of single photons by the X state and to an emission cascade of the XX state which can lead to polarisation entangled photon pairs in case the fine structure splitting of the intermediate X state is suitably small [43]. For applications, QDs are very interesting, as they can be embedded straightforwardly in diode structures enabling triggered electrical operation of the emitters [43]. Moreover, the radiative lifetime of QDs is below 1 ns enabling high photon generation rates beyond 1 GHz.

Due to the self-assembled epitaxial growth of the QDs deterministic nanoprocessing techniques are required for the fabrication of QD quantum light sources with high yield and optimal performance. Apart from site-controlled growth concepts, which usually lead to a trade-off between position control and optical quality of the QDs, in-situ lithography techniques are most promising for this purpose. Here, the pre-selection and the following lithographic definition of the photonic device structures are performed in one and the same apparatus without transferring the sample or heating it up. This has several appealing prospects: Firstly, the alignment accuracy is improved, as the coordinate system is identical for both steps. Secondly, it speeds up the fabrication, as no marker or coordinate-system matching is required for each write field. Not least, the technological complexity is strongly reduced, as only a single machine is necessary.

Besides optical in-situ lithography, in-situ electron beam lithography (EBL) is a very powerful deterministic device technology [44]. Here (see Figure 24), the sample is first spin-coated with an electron-beam resist at room-temperature. After cooling down the sample to cryogenic temperatures of about 10 K, pre-selection of target QDs based on their brightness and emission wavelength is performed by scanning the quantum emitters with the electron beam and mapping the luminescence using a spectrometer attached to the SEM. In the next step, the electron beam is used to define a photonic structure in the resist. As the resist is already exposed during the pre-selection process, the writing of the final structure is performed by inverting the resist, which directly acts as the etch mask for the final etch step after resist development at room-temperature. The overall lateral accuracy has been reported to be 34 nm [45], mainly limited by temperature-induced mechanical drifts of the sample holder inside the SEM and the process yield typically exceeds 90 %.

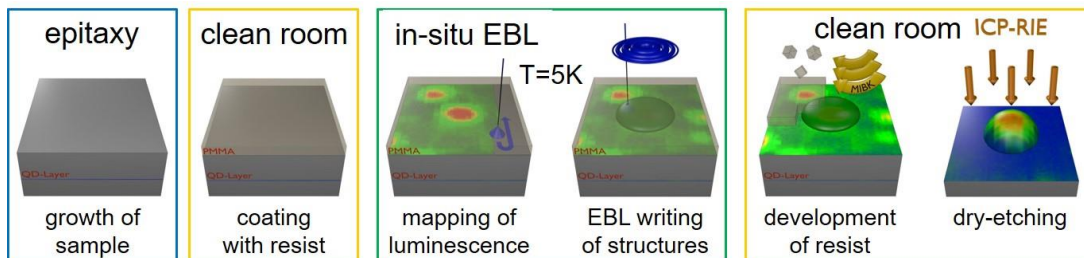


Figure 24: Full process flow for the deterministic structuring of an epitaxial semiconductor sample with integrated QDs via in-situ electron-beam lithography. A detailed description is given in the main text. (Parts are adapted from [46].)

Using in-situ EBL it is possible to realise three-dimensional photonic structures with enhanced photon extraction efficiency. Here, instead of using a fixed electron dose a variable dose in the negative-tone regime

<sup>43</sup> T. Heindel, C. Schneider, M. Lerner, S. H. Kwon, T. Braun, S. Reitzenstein, S. Höfling, M. Kamp, and A. Forchel, Electrically driven quantum dot-micropillar single photon source with 34% overall efficiency, *Appl. Phys. Lett.* 96, 011107 (2010)

<sup>44</sup> S. Rodt and S. Reitzenstein, High-performance deterministic in situ electron-beam lithography enabled by cathodoluminescence spectroscopy, *Nano Ex.* 2, 014007 (2021)

<sup>45</sup> M. Gschrey, R. Schmidt, J.-H. Schulze, A. Strittmatter, S. Rodt, S. Reitzenstein, Resolution and alignment accuracy of low-temperature in situ electron beam lithography for nanophotonic device fabrication, *J. Vac. Sci. & Techn. B* 33, 021603 (2015)

<sup>46</sup> M. Gschrey, A. Thoma, P. Schnauber, M. Seifried, R. Schmidt, B. Wohlfeil, L. Krüger, J. H. Schulze, T. Heindel, S. Burger, F. Schmidt, A. Strittmatter, S. Rodt, and S. Reitzenstein, Highly indistinguishable photons from deterministic quantum-dot microlenses utilizing three-dimensional in situ electron-beam lithography, *Nat. Commun.* 6, 7662 (2015)

of the resist (grey-scale lithography) is used to realise curved surfaces of the photonic structure hosting the single quantum emitter. This allows one to deterministically fabricate a photonic microlens with a single embedded QD acting as a bright single photon source. Combined with a backside DBR such devices show broadband photon extraction efficiencies of about 25 % into a numeric aperture (NA) of 0.4 [46], where the photon extraction efficiency refers to the fraction of the total photon flux emitted by the emitter which is collected by a lens with a given NA.

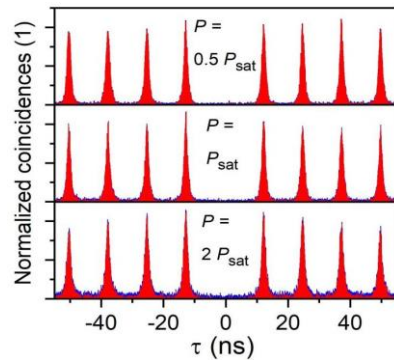


Figure 25: Photon auto-correlation measurements performed on a QD-microlens for different excitation powers relative to the saturation power of the  $X^+$  emission. All cases result in a  $g^{(2)}(0) < 0.01$ . (Adapted from [46].)

Another crucial parameter of single-photon sources is the multi-photon emission probability which is measured by the second-order photon autocorrelation function at zero delay  $g^{(2)}(0)$ . In the case of QD-microlenses low multi-photon emission probabilities  $g^{(2)}(0) < 0.01$  were observed (see Figure 25) which nicely reflects the high quantum-optical quality of these devices [45]. Even more important for many advanced applications of single-photon sources in photonic quantum technologies is the photon indistinguishability which corresponds to the mean wavefunction overlap of two photons from a statistical ensemble. Photons are called fully indistinguishable, if they can be described by the same set of identical quantum numbers. The photon indistinguishability can be determined via two-photon interference experiments in a Hong-Ou-Mandel (HOM) type setup. Here, two photons enter a 50:50 beamsplitter from different ports and interfere with each other. In case of perfect indistinguishability, both photons always leave the beamsplitter via the same, but stochastically random exit port, as the probability amplitudes destructively interfere for the cases where both photons are transmitted or reflected. This HOM effect can be observed as antibunching in coincidence measurements at both exit ports. In contrast to the antibunching in photon autocorrelation measurements, the photon indistinguishability is crucially affected by decoherence. Typically, two measurements are performed to experimentally determine the photon indistinguishability, one where the input photons have parallel polarisation orientation and the other one with orthogonal polarisation configuration. The contrast or visibility between both measurements reveals the photon indistinguishability.

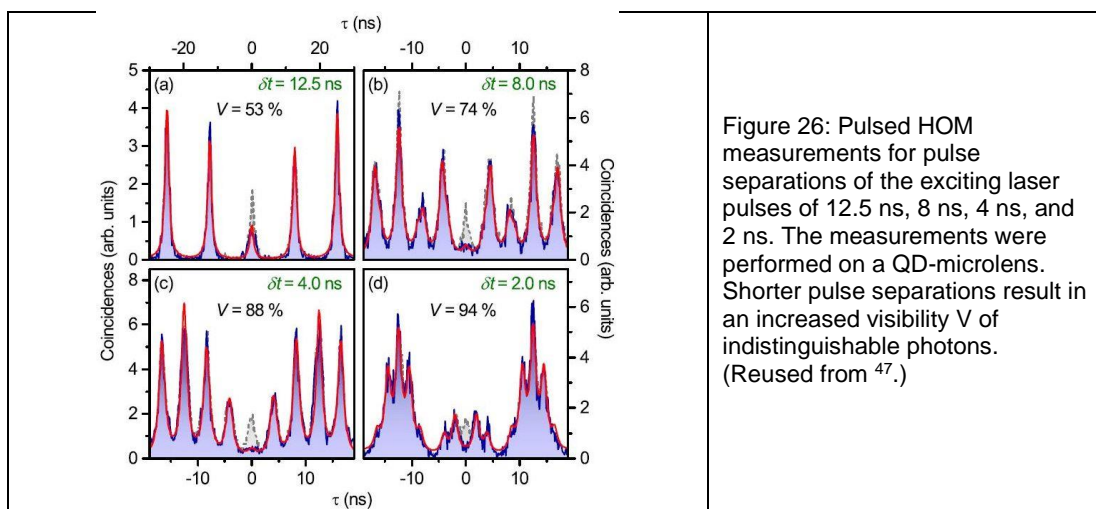


Figure 26: Pulsed HOM measurements for pulse separations of the exciting laser pulses of 12.5 ns, 8 ns, 4 ns, and 2 ns. The measurements were performed on a QD-microlens. Shorter pulse separations result in an increased visibility  $V$  of indistinguishable photons. (Reused from <sup>47</sup>.)

<sup>47</sup> A. Thoma, P. Schnauber, M. Gschrey, M. Seifried, J. Wolters, J.-H. Schulze, A. Strittmatter, S. Rodt, A. Carmele, A. Knorr, T. Heindel, and S. Reitzenstein, Exploring dephasing of a solid-state quantum emitter via time- and temperature-dependent Hong-Ou-Mandel experiments, Phys. Rev. Lett. 116, 033601 (2016)

QD-microlenses are good test objects to explore different mechanisms of dephasing, limiting the indistinguishability of photons emitted by the quantum emitter. In particular it was found that the two-photon interference visibility decreases with increasing temporal separation between consecutively emitted photons (see Figure 26), which is theoretically described by a non-Markovian noise process. At short temporal separations (2 ns) and low temperatures (10 K) photon indistinguishability of up to 96 % was observed under quasi-resonant excitation of the quantum emitter [47].

Besides microlenses, other nanophotonic structures have been proven to enable high-quality quantum emitters based on single QDs, too. Micro cavities based on micro pillars with a top and bottom DBR were among the first structures to enable efficient quantum emitters [48]. Recently, 4-photon cluster states were demonstrated via a deterministically fabricated micro pillar [49]. Circular Bragg gratings (CBGs) allow for combined high photon-extraction efficiency, entanglement fidelity and photon indistinguishability [50]. Besides these monolithic structures, an open-cavity approach was shown to enable tunable emission energy in combination with high indistinguishability and efficient fibre coupling [51].

Another interesting aspect is the generation of polarisation entangled photon pairs via the XX-X cascade of QDs. The corresponding entanglement fidelity  $F^+$  is defined as the overlap of an experimentally generated two-photon wavefunction  $|\Phi\rangle$  with the maximally entangled Bell state  $|\Psi^+\rangle = \frac{1}{\sqrt{2}} (|H_{XX}H_X + V_{XX}V_X\rangle)$ . Note that this Bell state is entangled in the polarisation degree of freedom, while entanglement can also be realised in different degrees of freedom, also simultaneously [52]. Experimentally, the entanglement fidelity is determined using quantum tomography, where  $F^+=0.5$  corresponds to a perfectly polarisation-correlated, but classical, state and  $F^+=1$  to a maximally entangled state.

Employing resonant two-photon excitation of the XX-X cascade of a deterministically fabricated QD-microlens, Bounouar et al. reported the generation of a maximally entangled state (see Figure 27) [53]. Here, the oscillating temporal evolution of the polarisation-entangled photon pair state was observed for two different quantum emitters with a fine-structure splitting of 16  $\mu\text{eV}$  and 30  $\mu\text{eV}$ , respectively. Noteworthy, it is very challenging to simultaneously achieve high photon extraction efficiency, high photon indistinguishability and high entanglement fidelity in a single device. Recently this task has been mastered by Liu et al. using a deterministically fabricated solid-state-based entangled photon pair source comprising a single QD embedded in a circular Bragg resonator integrated on a broadband reflector [54]. The device, exploiting a broadband Purcell effect, enabled the generation of entangled photon pairs with a collection efficiency of 0.65(4), an entanglement fidelity of 0.88(2), and an indistinguishability of 0.901(3) and 0.903(3) for X and XX respectively.

<sup>48</sup> S. Reitzenstein and A. Forchel, Quantum dot micropillars, *J. Phys. D: Appl. Phys.* 43, 033001 (2010)

<sup>49</sup> D. Istrati, Y. Pilnyak, J. Loredó, C. Anton, N. Somaschi, P. Hilaire, H. Ollivier, M. Esmann, L. Cohen, L. Vidro, C. Millet, A. Lemaitre, I. Sagnes, A. Harouri, L. Lanco, P. Senellart, H. Eisenberg, Sequential generation of linear cluster states from a single photon emitter, *Nat. Commun.* 11, 5501 (2020)

<sup>50</sup> H. Wang, H. Hu, T.-H. Chung, J. Qin, X. Yang, J.-P. Li, R.-Z. Liu, H.-S. Zhong, Y.-M. He, X. Ding, Y.-H. Deng, Q. Dai, Y.-H. Huo, S. Höfling, C.-Y. Lu, and J.-W. Pan, On-demand semiconductor source of entangled photons which simultaneously has high fidelity, efficiency, and indistinguishability, *Phys. Rev. Lett.* 122, 113602 (2019)

<sup>51</sup> N. Tomm, A. Javadi, N. Antoniadis, D. Najer, M. Löbl, A. Korsch, R. Schott, S. Valentin, A. Wieck, A. Ludwig, and R. Warburton, A bright and fast source of coherent single photons, *Nat. Nanotechnol.* 16, 399 (2021)

<sup>52</sup> M. Prilmüller, T. Huber, M. Müller, P. Michler, G. Weihs, and A. Predojević, Hyperentanglement of Photons Emitted by a Quantum Dot, *Phys. Rev. Lett.* 121, 110503 (2018)

<sup>53</sup> S. Bounouar, C. de la Haye, M. Strauß, P. Schnauber, A. Thoma, M. Gschrey, J. Schulze, A. Strittmatter, S. Rodt, and S. Reitzenstein, Generation of maximally entangled states and coherent control in quantum dot microlenses, *Appl. Phys. Lett.* 112, 153107 (2018)

<sup>54</sup> J. Liu, R. Su, Y. Wei, B. Yao, S. F. C. da Silva, Y. Yu, J. Iles-Smith, K. Srinivasan, A. Rastelli, J. Li, and X. Wang, A solid-state source of strongly entangled photon pairs with high brightness and indistinguishability, *Nat. Nanotechnol.* 14, 586 (2019)

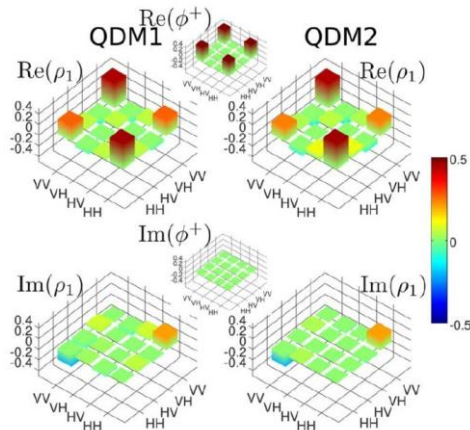


Figure 27: Quantum tomography measurements for two QD-microlenses (QDM1 and QDM2). Real parts are displayed on the top and imaginary parts on the bottom side. The small density matrices in the middle display theoretical real parts and imaginary parts of the maximally entangled state as a reference. (Reused from [53].)

In cases where the fine-structure splitting is large compared to the QD's homogenous linewidth, the polarisation entanglement between XX-X photon pairs will be washed out in time-integrated experiments. Still, the entanglement can be restored by temporal postselection, if the temporal resolution of the setup is sufficient. In fact, Huber et al. reported on polarisation-entangled photon pairs with a fidelity of 0.76 emitted by the XX-X cascade of a single QD despite a fine-structure splitting of 18  $\mu\text{eV}$  [55].

For practical applications it is very desirable to control the SPS' emission properties via external tuning "knobs". Prominent examples utilise electric fields [56] or temperature [57] to shift the emission energy, whereas the latter one is hardly applicable in practical applications. Another external tuning mechanism is based upon strain tuning that is realised by bonding the QD sample onto a piezoelectric actuator. This provides a versatile and reversible energy fine tuning that is highly suitable to bring different QDs into resonance (see Figure 28) [58].

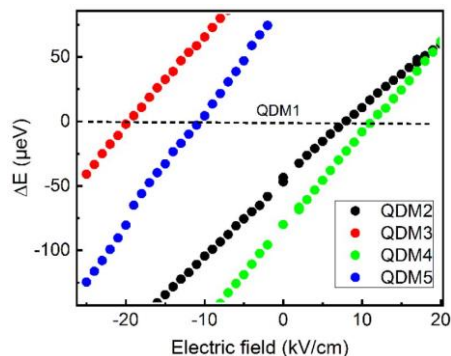


Figure 28: Strain-tuned emission energies of 4 QD-microlenses with respect to the emission energy of a reference QD-microlens (QDM1). All 4 QD-microlenses can be tuned into resonance for the respective electric field applied to the sub-mounted piezo actuator. (Reused from [58].)

Besides tuning the emission energy, it is of interest to control the emission dynamics, too. This way, the arrival time of single photons from different QDs might be synchronised or even 'stored' for a finite time span. This can be realised by light-matter interaction of single photons in dilute gas cells near absorption resonances of

<sup>55</sup> T. Huber, A. Predojević, M. Khoshnevar, D. Dalacu, P. Poole, H. Majedi, and G. Weihs, Polarization Entangled Photons from Quantum Dots Embedded in Nanowires, *Nano Lett.* 14, 7107 (2014)

<sup>56</sup> C. Kistner, T. Heindel, C. Schneider, A. Rahimi-Iman, S. Reitzenstein, S. Höfling, and A. Forchel, Demonstration of strong coupling via electro-optical tuning in high-quality QD-micropillar systems, *Opt. Express* 16(19), 15006 (2008)

<sup>57</sup> T. Farrow, P. See, A. J. Bennett, M. B. Ward, P. Atkinson, K. Cooper, D. J. P. Ellis, D. C. Unitt, D. A. Ritchie, and A. J. Shields, Single-photon emitting diode based on a quantum dot in a micro-pillar, *Nanotechnology* 19(34), 345401 (2008)

<sup>58</sup> M. Schmidt, M. V. Helversen, S. Fischbach, A. Kaganskiy, R. Schmidt, A. Schliwa, T. Heindel, S. Rodt, and S. Reitzenstein, Deterministically fabricated spectrally-tunable quantum dot based single-photon source, *Opt. Mater. Express* 10, 76 (2019)

the gaseous atoms. By guiding single photons from a QD microlens through a 150 mm Cs vapour cell, a total delay of 15 ns was demonstrated (see Figure 29) [59].

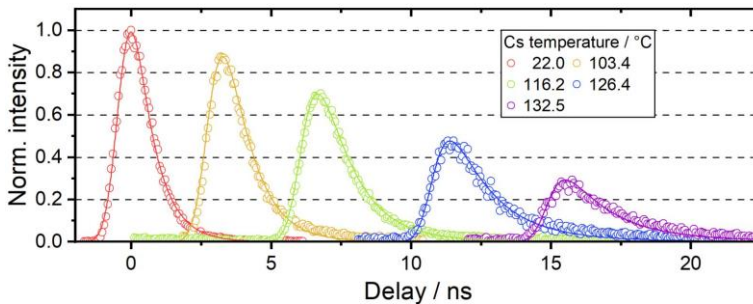


Figure 29: Photon delay in a 150 mm long Cs vapour cell for photons emitted from a QD-microlens. The energy difference between the QD's emission and the absorption energy of the Cs atoms is tuned by the temperature of the Cs gas. From the emission dynamics it is obvious that the emission process can be delayed by more than one order of magnitude. (Adapted from [59].)

For single molecules, indistinguishability of emitted photons was also demonstrated by CNR. A HOM interference visibility of more than 75 % is reported, limited by the residual dephasing present at the operating temperature of 3 K. A visibility of 96 % is expected for the very same experiment in the case of 1.5 K operation.

#### 4.3.2 Perspectives of sources of indistinguishable and entangled photons based on single photon sources in metrology

As was shown, SPSs capable of generating indistinguishable and entangled single photons are long-awaited building blocks for application in quantum technology such as e.g., quantum metrology and quantum cryptography. At the moment, sources of indistinguishable and entangled single photons have not entered European NMIs for metrological purposes. Therefore, metrological applications arising from the use of such sources have not been realised thus far. The work performed in the frame of this project, to establish sources of indistinguishable and entangled photons based on near infrared ( $< 1 \mu\text{m}$ ) quantum dot single-photon sources with a visibility  $> 90 \%$ , contributes to the advancement in single-photon metrology that is currently needed to bring those sources into the NMIs to form the basis for future work in the field of quantum-enhanced metrology. Sources of indistinguishable photons, such as the one based on QD microlenses (such as the one developed during the project), in particular, are extremely interesting for several applications ranging from quantum communication to the development of standard sources. Furthermore, sources that can emit entangled photons can open totally new fields in quantum metrology, since it is expected that novel sensing and measurement techniques based on these sources can be developed, increasing the measurement capabilities of metrological institutes.

The investigations for sources of indistinguishable and entangled photons operating in the telecom wavelength range around  $1.5 \mu\text{m}$  were carried out by USTUTT, see section 4.2.3.3,

#### 4.3.3 Novel sensing and measurement techniques

Optical Detection of Magnetic Resonance (ODMR) sensing protocols were developed with NV centres showing  $40 \text{ nT/Hz}^{1/2}$  magnetic sensitivity in continuous excitation ( $70 \text{ nT/Hz}^{1/2}$  in biocompatible conditions) by INFN, INRIM and UNITO. This is in line with the current state of the art for sensing volume, thus further work to increase the sensitivity and pulsed measurements is on-going. So far Rabi oscillations and Ramsey fringes have been observed and the first preliminary results of pulsed ODMR have shown improved linewidth of the resonance dip.

The project partners INRIM, TUB, UNITO have investigated a new paradigm dubbed the genetic quantum measurement. Specifically, the use of the genetic quantum measurement approach with QD and colour centres in diamond (objective 1) was studied in order to determine whether there is a specific observable in these quantum systems that can take advantage of the new genetic quantum measurement approach. The results showed that the polarisation degree of freedom is suitable and that the most suitable source for the polarisation degree of freedom is the single-photon source since it naturally emits photons in a defined linearly polarised

<sup>59</sup> L. Bremer, S. Fischbach, S.-I. Park, S. Rodt, J.-D. Song, T. Heindel, and S. Reitzenstein, Cesium-Vapor-Based Delay of Single Photons Emitted by Deterministically Fabricated Quantum Dot Microlenses, *Adv. Quantum Technol.* 3, 1900071 (2020)

state. Therefore, such a single-photon source has been used to investigate different regimes in terms of interaction strengths and polarisation states.

#### 4.3.4 Summary

Sources of indistinguishable and entangled photons based on near infrared ( $< 1 \mu\text{m}$ ) QD single-photon sources with a visibility  $> 90 \%$  were established. Novel sensing and measurement techniques based on single-photon sources were investigated. Also a new paradigm dubbed the genetic quantum measurement was investigated.

### 4.4 Objective 4

*To develop metrology infrastructure for traceable single-photon source characterisation, i.e. detectors, amplifiers, single-photon spectroradiometers.*

In the following, the setups developed or further developed within the SIQUST project are listed and described.

#### 4.4.1 Low optical flux detectors (LOFP)

A Si S1227 33 Hamamatsu Si photodiode is placed in a custom-made aluminium housing. One side of the housing is threaded to accept different types of commercially available fibre connectors. The mechanical set up is designed to place the fibre optic tip at a fraction of a millimetre from the photodiode sensitive area to guarantee that all the optical radiation is collected by the photodiode. The photodiode terminals are connected to a SIA developed by CMI<sup>[60]</sup> equipped with a 1pF Mica integration capacitor. The value of the capacitor has been calibrated using the method described in<sup>[61]</sup>. Changing the integration time of the SIA the I/V conversion factor can be set to a value that ranges from  $1 \times 10^9$  to  $1 \times 10^{12}$ .

For a monochromatic source of wavelength  $\lambda$  the number of photons per unit of time impinging the LOFP's photodiode is calculated by the equation  $N_{\text{photons/s}} = (V_{\text{out}} \times C_{\text{int}}) / (R_{\lambda} \times t_{\text{int}} \times e_{\lambda})$ , where  $R_{\lambda}$  is the responsivity of the photodiode at  $\lambda$  and  $e_{\lambda}$  is the energy of a photon at  $\lambda$ .

The absolute spectral responsivity of the LOFP's Si photodiode has been calibrated using the CMI double monochromator facility. The LOFP and the CMI Si trap transfer standard detector were alternatively illuminated by the spectrally selected light. The CMI trap detector is directly traceable to the CMI primary standard for optical radiation, the cryogenic radiometer. The calibration has been performed in the spectral range 580 nm – 960 nm, with 10 nm steps, with power levels of a few nW in order not to saturate the CMI detector set to its lowest sensitivity. The total expanded uncertainty of the spectral responsivity above 900 nm is about 2.2 %. A series of measurements of the photon flux emitted by the PTB single-photon source were performed with the LOFP at different optical excitation levels for the SPS. The relative standard deviation of five measurements with the SPS photon flux of about  $1.2 \times 10^6$  photons/s and  $0.4 \times 10^6$  photons/s, are 1 % and 1.7 %, respectively. Note that the statistical scatter values reported include both the random detector noise and the SPS flux fluctuations. The fact that the total relative noise does not scale with the photon flux indicates that the LOFP noise floor contribution is not dominant to the overall measured noise.

#### 4.4.2 Predictable quantum efficient detector for traceable low optical flux measurements of SPS systems

The predictable quantum efficient detector (PQED) is a primary standard of optical power operating in the visible wavelength range<sup>[62]</sup>. The PQED consists of two custom-made induced-junction silicon photodiodes arranged in a wedged trap configuration. Originally, all PQED photodiodes were based on a structure of thermally grown silicon oxide ( $\text{SiO}_2$ ) on p-type silicon. Recently, an alternative structure was demonstrated<sup>[63]</sup>, where atomic layer deposition (ALD) was used to grow aluminium oxide ( $\text{Al}_2\text{O}_3$ ) on top of n-type silicon. Two sets of n-type silicon induced-junction photodiodes were manufactured, denoted as set A and B, with

<sup>60</sup> Mountford, J., Porrovecchio, G., Smid, M., Smid, R.: Development of a switched integrator amplifier for high-accuracy optical measurements. *Appl. Opt.* 47(31), 5821 (2008)

<sup>61</sup> Porrovecchio, G., Smid, M., Lopez, M., Rodiek, B., Kück, S., Hofer, H., Comparison at the sub-100 fW optical power level of calibrating a single-photon detector using a high-sensitive, low-noise silicon photodiode and the double attenuator technique. *Metrologia* (53), 1115-1122 (2016).

<sup>62</sup> Sildoja, M., Manoocheri, F., Merimaa, M., Ikonen, E., Müller, I., Werner, L., Gran, J., Kübarssepp, T., Smid, M., Rastello, M.L.: Predictable quantum efficient detector: I. Photodiodes and predicted responsivity. *Metrologia* 50(4), 385 (2013)

<sup>63</sup> Dönsberg, T., Mäntynen, H., Ikonen, E.: Optical aperture area determination for accurate illuminance and luminous efficacy measurements of LED lamps. *Opt. Rev.* 23(3), 510 (2016)

respective doping concentrations of  $2.5 \times 10^{11} \text{ cm}^{-3}$  and  $4.4 \times 10^{11} \text{ cm}^{-3}$ . In addition to a smaller doping concentration, set A photodiodes have 16 guard rings, whereas those of set B have only one. These factors lead to a decrease of dark current by a factor of five at room temperature for the set A photodiodes when compared against set B [63]. Improved dark current characteristics play a major role in low optical flux measurements, as reduced dark current will increase the signal-to-noise ratio (SNR). Additionally, simulations have been carried out to determine dark current behaviour when cooling the photodiodes down to cryogenic temperatures [64, 65]. These simulations indicate that the dark current will decrease exponentially with lowering temperature. Thus, cooling the PQED would drastically increase the dynamic range of the PQED, and would enable the PQED to be used as a primary standard in single and few photon applications [66]. Manoocheri et al., have reported the design of a cryogenic PQED consisting of a liquid nitrogen (LN) cooled cryostat fitted with n-type photodiodes [67]. Porrasmaa et al., have reported the dark current dependence on bias voltage at room temperature for both the n- and p-type PQED photodiodes. The dark current properties of the n-type detector in the temperature range of 76–300 K have also been presented and demonstrated the possibility of using the PQED as a primary standard in low flux applications [68].

The measurements have been carried out with a similar setup as described in [63] with the addition of the cryostat on the XY-translation stage and neutral density (ND) filters for attenuating the incident laser beam. For measuring the dark current and low flux photocurrent, the photodiodes were connected to a precision, gain-controllable, commercial transimpedance amplifier (TIA). Two ND filters with nominal optical densities of 3.0 and 4.0 were used to reduce the power of the stabilised laser beam down to 2.8 pW. This corresponds to roughly 7,000,000 photons per second at a vacuum wavelength of 488.12 nm. While the responsivity simulation of the PQED assumes reverse bias [68], at such a small power level, the uncertainty due to non-biased operation is significantly less than the uncertainty of the measurements [63]. Thus, the photodiodes were not biased. This increased the SNR (lowers the noise floor) significantly. In optical power measurement at 76 K and without biasing, a relative standard uncertainty of 0.15% was achieved within a 5-min measurement period.

#### 4.4.3 *Transmission-type photodetectors as an alternative attenuator to achieve and monitor low photon flux*

In the establishment of the traceability of low photon flux detectors to primary standards (e.g., cryogenic radiometer, Predictable Quantum Efficiency Detector) optical filters or other optical components are often used. One of the drawbacks in using additional optical components is undesired back-reflection, which can cause inter-reflections and stray light in the measurement system and, as a consequence, an increase in uncertainty. One way to overcome this is to use a special type of attenuator, so-called transmission type detectors, developed within his project by Metroser. The photodiodes used in the transmission type detector (further called as detector 6X) are Silicon-photodiodes type S1227-33 SPL (windowless) from Hamamatsu with an active area 2.4 mm × 2.4 mm. This type of photodiode has been proved to operate at low noise and high sensitivity and has been used to establish reliable traceability chain to the cryogenic radiometer in low photon flux measurements [61]. The alignment of six photodiodes was chosen in such a way that it provides almost collinear input and output beams, and transmittance, as well as responsivity are independent of the polarisation state of the beam [69] (Figure 30a). The configuration of the photodiodes was designed for the shortest optical path 38 mm in the device, limited mostly by the photodiode's frame dimensions and the piezo-mover, holding one of the photodiodes for fine tuning purposes of the beam travelling between the photodiode active surfaces (Figure 30b). The outer housing of the transmission type detector 6X is rectangular in shape in which the total optical path is 103 mm. The Peltier' element type TECL4 in conjunction with thermocontroller TED200C from

<sup>64</sup> Manoocheri, F., Sildoja, M., Dönsberg, T., Merimaa, M., Ikonen, E.: Low-loss photon-to-electron conversion. *Opt. Rev.* 21(3), 320 (2014)

<sup>65</sup> Geist, J., Brida, G., Rastello, M.L.: Prospects for improving the accuracy of silicon photodiode self-calibration with custom cryogenic photodiodes. *Metrologia* 40(1), S132 (2003)

<sup>66</sup> Vaigu, A., Porrovecchio, G., Chu, X.L., Lindner, S., Smid, M., Manninen, A., Becher, C., Sandoghdar, V., Göttinger, S., Ikonen, E.: Experimental demonstration of a predictable single photon source with variable photon flux. *Metrologia* 54(2), 218 (2017)

<sup>67</sup> Manoocheri, F., Dönsberg, T., Sildoja, M., Smíd, M., Porrovecchio, G., Ikonen, E.: Liquid nitrogen cryostat for predictable quantum efficient detectors. *J. Phys. Conf. Ser.* 972(1), 012021 (2018)

<sup>68</sup> Porrasmaa, S., Dönsberg, T., Manoocheri, F., Ikonen, E., "Predictable quantum efficient detector for low optical flux measurements", *Optical Review* (2020) 27:190–194 <https://doi.org/10.1007/s10043-020-00580-1>

<sup>69</sup> T Kübarssepp et al (1996), Characterization of a polarization-independent transmission trap detector, *Appl Opt*, 36, pp 2807-2812

Thorlabs is used to cool the detector 6X. The feedback thermistor type AD590 is located close to the mechanical body holding the photodiodes in the designed configuration.

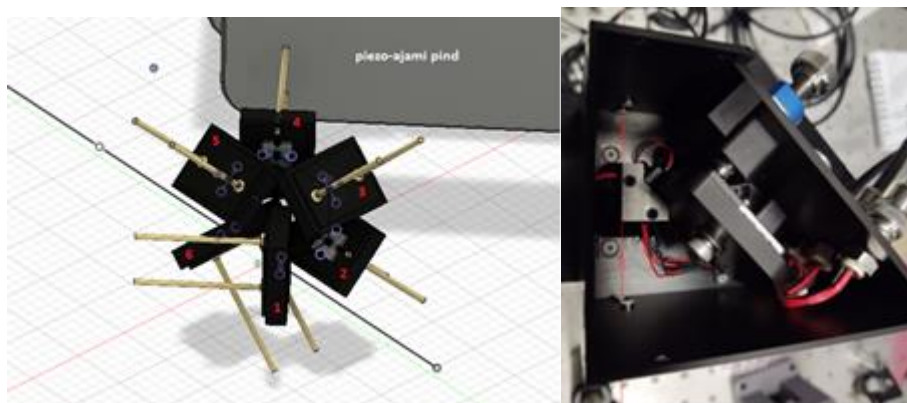


Figure 30. a) The schematic isometric view of six photodiodes in the transmission trap detector. b) Top view of the transmission trap detector with the top lid opened.

The active area of the detector 6X was measured using a 676-nm laser wavelength beam with a diameter of about 1 mm. The measurements were performed with scan step of 0.25 mm at room temperature. The active area of the photodetector 6X is about 1.75 mm (height) and 1.25 mm (width).

By knowing the thickness of the SiO<sub>2</sub> antireflection coating on the top of the Si-photodiode active surfaces, the fraction of the incoming beam transmitted through the detector (i.e., attenuated) can be estimated. The previous studies have indicated that the antireflection coating thickness of photodiodes type S1227-33 is  $t = (30 \pm 1) \text{ nm}$  [70]. At the laser wavelength of 639 nm, the expected transmittance is  $7.51 \times 10^{-4}$ , i.e., the attenuation is 1331 times, the measured transmittance is  $7.65 \times 10^{-4}$ , i.e., the attenuation is 1307 times. The transmittance of the detector 6X was also measured when the device was cooled from room temperature to +12 °C. The optical power in the transmitted beam drops by about  $4 \times 10^{-6}$  within the first 15 minutes of detector cooling. After that, the transmittance is stable, to be better than  $\pm 2 \times 10^{-6}$  during the 1 hour cooling process of the detector 6X. This, probably, indicates that the cooling of the detector did not cause significant displacement of the individual photodiodes in the device.

The photodetector 6X can be cooled from laboratory temperature + 22.9 °C to + 12 °C within 1¼ hours. The dark current measurements were conducted in the temperature range from +15°C to +23°C. The dark current reading from photodiodes 1, 2, 5 and 6 of the photodetector 6X summed up was registered by using a conventional current-to-voltage amplifier with a gain setting of 10<sup>9</sup>. The dark current of photodiodes 1, 2, 5 and 6 decreases by about 25 fA/°C. The total dark photocurrent of the detector 6X was measured at temperatures +15 °C and +23 °C using different amplifier gain settings: 10<sup>4</sup>, 10<sup>7</sup> and 10<sup>9</sup>. It was observed that the dark current of the detector at temperature +15 °C is about one order of magnitude less as compared to that at temperature +23 °C at three amplifier gain settings.

The responsivity of the detector 6X was calibrated against PQED at the laser wavelengths of 647 nm and 676 nm by using the 1-mm diameter of the laser beam at Aalto and VTT. The responsivity of detector 6X was measured to be 0.506 A/W and 0.520 A/W, respectively. The results at different levels of the optical power at two temperatures indicate that the responsivity of detector 6X is stable regardless of the level of optical power and temperature.

#### 4.4.4 Single-photon source characterisation facilities

##### 4.4.4.1 Characterisation facilities for single-photon sources based on impurity centres in diamond

Diamond as a host medium for single-photon emitters is advantageous because of the mechanical stability and the possibility to generate single-photons at room temperature. Impurity-based centres such as germanium-vacancy, tin-vacancy and nitrogen-vacancy centres are candidates for applications using single-photon sources at room temperature. These emitters, fabricated by INFN, INRIM and UNITO, are characterised in a self-built confocal microscope setup at PTB, which is illustrated in Figure 31.

<sup>70</sup> A Pokatilov et al, Low-noise miniature photodetector as a transfer standard for SPAD calibration in the visible wavelength range, Proc. of NEWRAD 2017 (Tokyo, Japan, 2017)

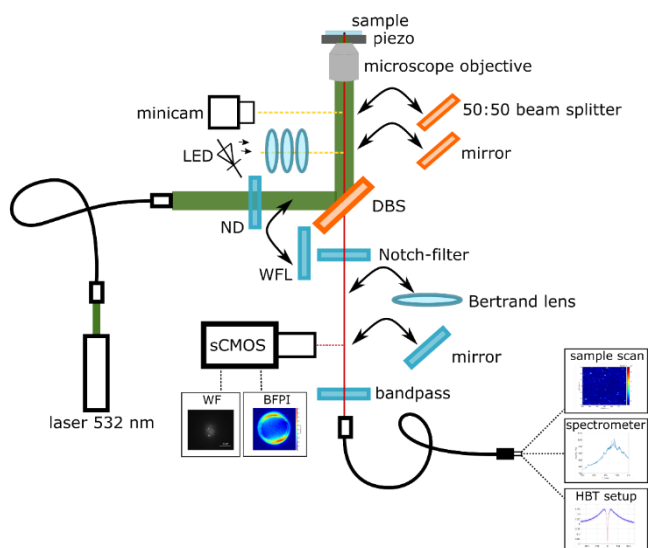


Figure 31. Confocal microscope setup to characterise single-photon emitters in diamond at room temperature. ND: neutral density filter. WFL: wide-field lens. DBS: dichroic beam splitter.

The laser light at 532 nm (PicoQuant, LDH-D-FA-530L) with a maximum CW power of up to 5 mW or pulsed operation with up to 80 MHz repetition rate is coupled into the microscope setup using a single-mode optical fibre (Thorlabs, P1-460-FC-2) and attenuated by a neutral density filter wheel called (Thorlabs, NDC-100C-4M). A dichroic beam splitter (Thorlabs, DMLP550) is used to direct the laser onto the microscope objective (Olympus, MPlan Apo N, 50x NA 0.95, can be exchanged with Mitutoyo, M Plan Apo 100x NA 0.7). Using a piezo translation stage (PI, P563.3CD), the sample can be scanned in three dimensions. The fluorescence from the focal volume is gathered by the same microscope objective and filtered by a Notch-filter (Edmund Optics, 532 nm Notch-filter, OD6, #86-130) and a bandpass filter (Edmund Optics, 620nm bandpass, 56 nm bandwidth, OD6, #33-910) for germanium-vacancy or tin-vacancy centre samples or long-pass and short-pass filters (Thorlabs, FEL600 and FES700) for nitrogen-vacancy centres. A single-mode optical fibre (Thorlabs, P1-630A-FC-2) is used as the pinhole. The fluorescence is then measured in a single-photon avalanche diode (Laser Components, Count-T-100-FC), a HBT setup consisting of two detectors and a beam splitter (Thorlabs, TW670R5F1) or a spectrometer (Princeton, Spectra Pro SP-2500). The setup also has the possibility for wide-field microscopy of the fluorescence and back focal plane imaging using a sCMOS camera (Andor, Zyla 4.2Plus). An LED and a minicam (Thorlabs, DCU223M) are used to align the sample with the microscope objective.

Nanodiamonds that were spin-coated onto a cover glass emit more than 80 % of their photons into the cover glass [71]. The extraction efficiency of the photons from the cover glass is enhanced by using oil-immersion microscope objectives, since no total internal reflection in the cover glass can occur. Therefore, the microscope objective in the setup can be exchanged with an oil-immersion objective (Nikon, CFI Plan Apochromat Lambda 60x Oil).

#### 4.4.4.2 Characterisation facilities for single-photon sources based on InGaAs quantum dots in the near infrared spectral range

Semiconductor quantum dots are robust and mechanically stable. They can endure many cooling cycles, and they do not suffer from blinking and photobleaching. Another advantage is the short decay time in the order of 1 ns which allows for pulsed excitation at high repetition frequencies. In the following, a non-resonant optical excitation at a frequency of 80 MHz is applied at the PTB setup for the sources provided by TUB.

A key technique for the optical characterisation of semiconductor quantum dots and other quantum emitters in general is confocal fluorescence microscopy. The confocal setup is illustrated by a schematic sketch in Figure 32. The setup transmission is optimised for the emission wavelength of the quantum dots (around 930 nm). Furthermore, the setup is equipped with a helium flow cryostat for cooling the sample to cryogenic temperatures.

<sup>71</sup> J. Christinck et al., Appl. Phys. B. 126, 161 (2020)

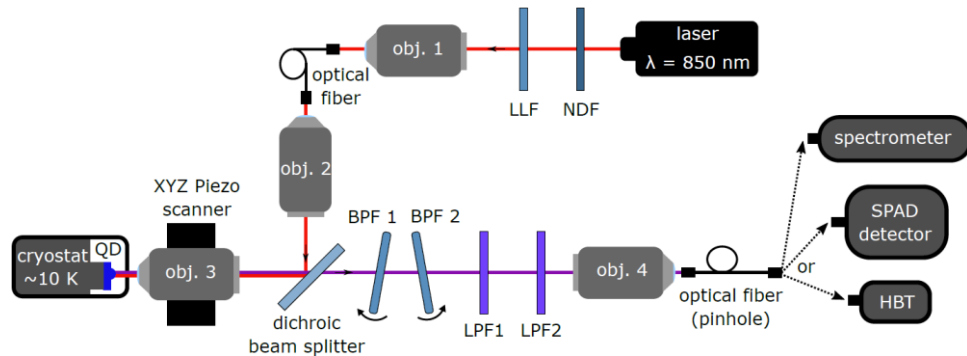


Figure 32. Sketch of the confocal setup for the optical characterisation of semiconductor quantum dots emitting at around 930 nm. The excitation beam passes through a neutral density filter (NDF) and a laser line filter (LLF). Then it is reflected at the dichroic beam splitter and focused on the sample by objective 3. The sample is cooled down to about 10 K via a helium flow cryostat. The fluorescent emission is spectrally filtered by two bandpass filters (BPF1 and BPF2) and two long pass filters (LPF1 and LPF2). Objective 4 focuses the light beam into an optical fibre that serves as a pinhole and can be connected to either a spectrometer, a SPAD detector or a Hanbury-Brown and Twiss (HBT) interferometer. Taken from [72].

The excitation laser (PicoQuant, LDH-D-C-850) in pulsed mode has a relatively broad spectral emission, which has to be constrained by a laser line filter (LLF) at  $850 \pm 10$  nm. Moreover, the excitation power is adjusted with a neutral density filter (NDF) wheel (Thorlabs, NDC-100C-4M). The same objective (obj. 3) is used to focus the excitation beam on the sample and to collect the fluorescent emission. A dichroic beam splitter (Semrock, 875 nm edge BrightLine) separates the fluorescent beam from the excitation beam. Two long pass filters (LPF, Thorlabs, FEL0900 and Edmund Optics, high performance OD 4.0) with a cut-off wavelength of 900 nm additionally suppress the laser beam. The spatial filtering in front of the detector is realised by an optical fibre, which has the function of a confocal pinhole that filters out light originating outside the focal spot.

The sample is raster-scanned point by point to construct a two-dimensional fluorescence image, as shown in Figure 33a. The fluorescent light is detected by a single-photon avalanche detector (SPAD) with a sensitivity at the single-photon level. The selected quantum emitter in the scan is placed in focus. Then the optical fibre is connected to a spectrometer to obtain the spectral characteristics. The spectral filtering of the quantum dot emission is realised by two very narrow bandpass filters (BPF, Alluxa, 935.0–0.45 OD5) mounted on automated rotation stages (PI, RS40 with a Mercury C-863 DC motor controller). A wavelength shift of the central wavelength of the transmission window as a function of the incident angle is expected. This shift is implemented for the spectral selection of a specific emission line with an emission wavelength close to the target value of 930 nm (see Figure 33b).

The last characterisation step consists of analysing the single-photon purity by a measurement of the second-order correlation function. This measurement is performed with a Hanbury Brown and Twiss interferometer made of a 50/50 fibre-based beam splitter (Newport, F-CPL-M12855) with multimode fibres having a core diameter of 62.5  $\mu\text{m}$ , two Si-SPADs and electronics (PicoQuant, PicoHarp 300) for time-correlated single-photon counting (TCSPC). The  $g^{(2)}(0)$  values at different photon fluxes are shown in Figure 33c. Photon fluxes of up to approx. 2.6 million photons per second at the position of the single-photon detector were achieved.

<sup>72</sup> H. Georgieva et al. Opt. Express 29 15 (2021)

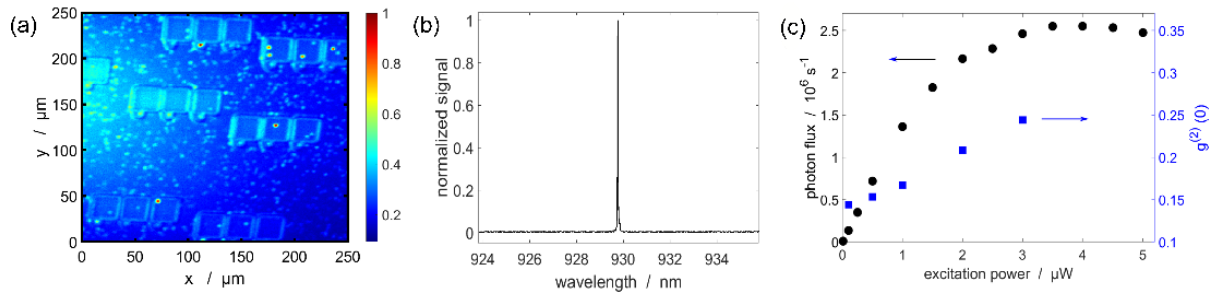


Figure 33. a) Micro-photoluminescence scan of the sample emission. Emission below 900 nm is filtered out by a long pass filter. B) Spectrum of the quantum dot emission with applied spectral filtering. C) The black circles indicate the photon flux arriving at the single-photon detector as a function of the excitation power, whereas the blue circles indicate the corresponding  $g^{(2)}(0)$  values. Figure c) is taken from [72].

The metrological characterisation requires traceability to the primary standard for optical power, the cryogenic radiometer. Therefore, the use of calibrated SPAD detectors enables absolute measurements of the photon flux and of the corresponding optical power. An important advantage of InAs quantum dots is their narrow-bandwidth emission. A monochromatic emission is an essential prerequisite for the calibration of light detectors, whose detection efficiency strongly depends on the wavelength. During the SIQUEST project, PTB performed a relative calibration [73], carried out with the fibre exchange technique, that reached a relative standard uncertainty of 0.7 % for the ratio of detection efficiencies of two SPADs. Moreover, an absolute calibration [72] was demonstrated by a direct comparison of a SPAD with a low noise analogue detector via the substitution method. At high photon fluxes, the diminished nonlinearity of the apparent detection efficiency due to the sub-Poisson statistics proved the advantage of semiconductor quantum dots over laser light for applications in the field of quantum radiometry.

#### 4.4.4.3 Characterisation facilities for single-photon sources based on InGaAs quantum dots in the infrared spectral range

The sample characterisation facility being established and verified at NPL is schematically outlined in Figure 34. Some incidental optics such as mirrors to facilitate alignment and coupling lenses for the imaging spectrometer have been omitted to aid schematic clarity.

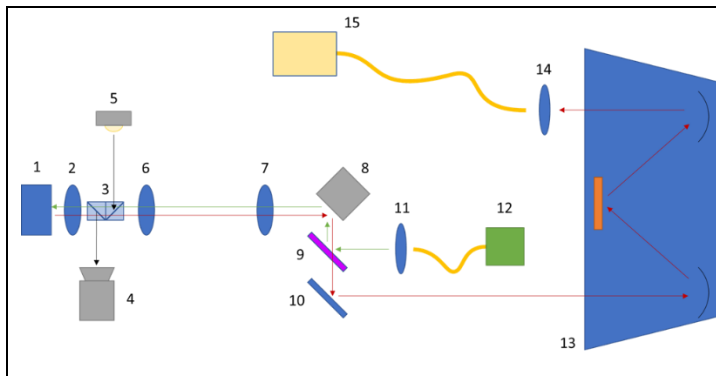


Figure 34. The experimental apparatus to perform measurements on QDs in the telecoms C band. 1. Continuous flow cryostat. 2. Aspheric (objective) lens. 3. Beam splitter pair for widefield imaging (removed during single photon data acquisition). 4. CMOS camera. 5. White LED. 6. Telecentric lens. 7. Telecentric lens. 8. Fast steering mirror. 9. Dichroic mirror. 10. Enhanced IR Au mirrors. 11. 850 nm collimation lens. 12. Fibre coupled 850 nm source. 13. Czerny-Turner spectrometer (iHR550). 14. Focussing lens for SMF28 fibre. 15. Multi-channel SNSPD system.

The system is designed to couple fluorescence from the quantum dot (QD) source to a set of superconducting nanowire single-photon detectors (SNSPDs). The sample is housed in a continuous flow cryostat (Janis ST-500), labelled (1) in Figure 34. Emission from the cryostat is coupled into a 0.55 N.A. aspheric lens (Thorlabs AL1512-C), (2 in Figure 34). A pair of beam splitter cubes (3) can be inserted into the optical path for sample positioning. This allows white light (5) to be coupled in, and a wide field image to be projected onto the CMOS camera (4). Once the sample is correctly positioned these are removed, decoupling the camera and white light source from the system. A scanning mechanism comprised of two telecentric lenses (Thorlabs AC508-150-C-ML) are positioned in a 4-f arrangement (6,7). This allows the fast-steering mirror (Newport

<sup>73</sup> H. Georgieva et al. Metrologia 57 5 (2020)

FSM), (8) to raster the angle of incidence of the optical path, scanning the focal region of the aspheric objective lens. A dichroic mirror (Thorlabs DMLP1180R), (9) couples the excitation source into the system. This is a CW 850 nm laser diode (Thorlabs LP852-SF30), (12), collimated by lens (11). Mirrors (10) couple the light into an imaging spectrometer (Horiba iHR550). Here the grating (600 lines/mm, 1000 nm blaze) can be used to spectrally select transmission lines or use the 0<sup>th</sup> order for imaging. The transmitted fluorescence is then coupled into an SMF28 fibre by a focussing lens (14), which is coupled to an SNSPD system (PhotonSpot).

The system is currently in the final stages of alignment and verification and should yield results in the near future.

#### 4.4.4.4 Characterisation facilities for single-photon sources based on molecules

The general characteristics of molecule based single-photon sources have been described in section 4.1.3. The setup for the characterisation, as established at CNR, consists of a simple epi-fluorescence microscope, and is depicted in Figure 35. In this setup, different types of molecule-based emitters and devices may be placed, provided that spectrally suitable lasers for excitation and optics, especially the dichroic beam splitter, are available.

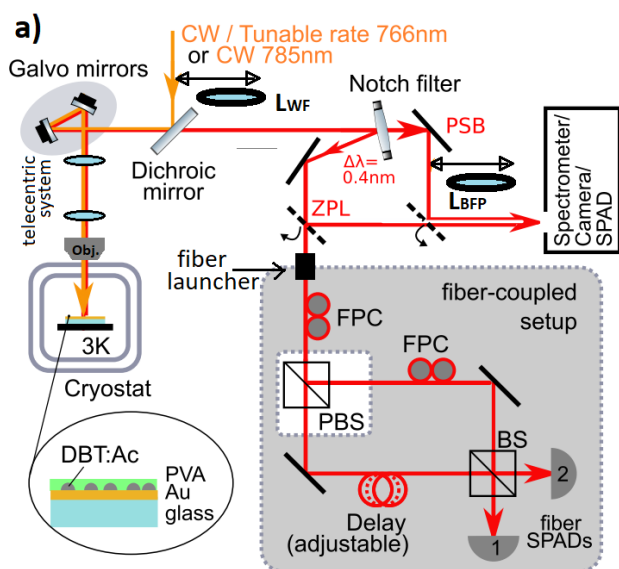
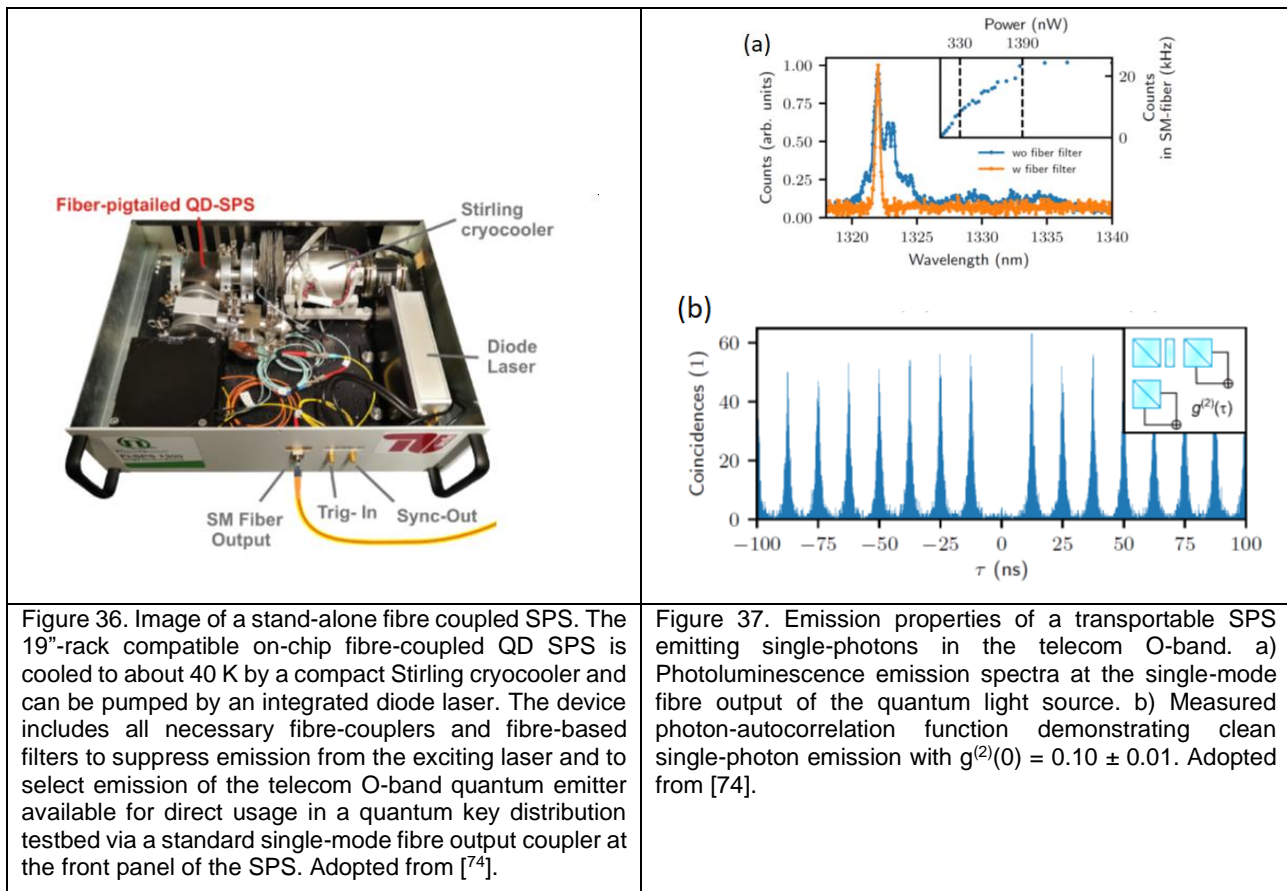


Figure 35. Sketch of the setup for the characterisation facilities for single-photon sources based on molecules. FPC: fibre polarisation controller, (P)BS: (polarising) beam splitter, LBFP: back focal plane lens, LWF: wide field imaging lens, PVA: polyvinylalcohol, DBT:AC: dibenzoterrylene in anthracene.

#### 4.4.5 Transportable single photon sources

##### 4.4.5.1 Transportable single-photon source based on semiconductor quantum dots

Compact and user-friendly single-photon sources (SPSs) are key building blocks in photonic quantum technologies. In the best case they provide single photons on-demand at telecom wavelengths via single mode fibres. To reach this challenging goal, TUB developed InGaAs quantum dot (QD) based single-photon sources that can be used in a plug & play fashion with emission at around 930 nm and in the telecom O-band at 1.3  $\mu\text{m}$ . The sources are on-chip fibre-coupled and are cooled by a compact Stirling cryocooler for stand-alone operation, see picture in Figure 36. The emission properties of the stand-alone single-mode fibre-coupled QD SPS emitting in the telecom O-band are presented in Figure 37. Panel a) compares the emission detected at the fibre-output of the source with (orange trace) and without the integrated fibre-based bandpass filter (full-width at half maximum: 0.5 nm). With an installed filter very clean emission at the target emission wavelength in the telecom O-band is observed. The count rate at the output of the single-mode fibre output depends on the excitation laser power and reaches close to 25 kHz at about 5  $\mu\text{W}$ . Panel b) presents results on the single-photon emission properties of the source under pulsed quasi resonant p-shell excitation. The measured photon-autocorrelation functions show very pronounced photon anti-bunching associated with  $g^{(2)}(0) = 0.10 \pm 0.01$ . This reflects the excellent quantum nature of emission of the stand-alone SPS.



The achieved results clearly highlight the high potential of QD based structures to act as portable SPSs for applications in quantum metrology and quantum communication. Further optimisation will focus on maximising the single-photon flux by improving the fibre-coupling efficiency and to further improve the quantum nature of emissions also in terms of high photon indistinguishability.

#### 4.4.5.2 Transportable single-photon source based on molecule and impurity centres in diamond

A compact single-photon source was developed by FAU and metrologically characterised by PTB within the frame of the SIQUEST project. It basically consists of a compact confocal setup that uses a NV-Centre or a single molecule as a single-photon emitter. The setup is shown in Figure 38. Here a continuous wave (CW) laser with a wavelength of 532 nm is used for the excitation of the single-photon emitters. The laser beam is spectrally cleaned using a laser line filter and directed through a dichroic mirror to the microscope objective. The microscope objective focuses the excitation beam onto the sample or is used in a total internal reflection configuration. The fluorescent light emitted by the emitter is then collected using the same microscope objective and it passes through the dichroic mirror and long-pass filter to filter out the excitation laser. The beam is magnified using a 2:1 telescopic assembly, which also has an optional slot for a pinhole, and is then guided to an EMCCD camera or coupled via a lens to a multimode optical fibre. The single-photon purity of the emitters is determined by an Hanbury Brown & Twiss (HBT) interferometer, which consists of a fibre beam splitter and two SPD modules. Thus, the single-photon emission is provided to the users via a MM fibre optic.

<sup>74</sup> L. Bremer et al., Quantum dot single-photon emission coupled into single-mode fibers with 3D printed micro-objectives, APL Photonics 5, 106101 (2020)

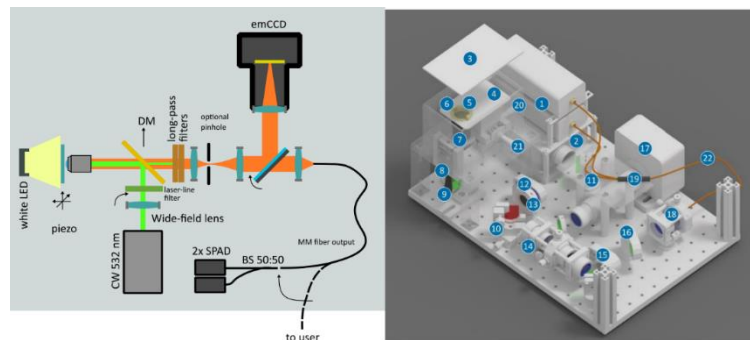


Figure 38. Left: Scheme of the compact single-photon setup. Right: Physical layout of the setup. Elements: 1) SPAD detectors, 2) excitation laser, 3) cover lid with LED illumination, 4) sample holder plate, 5) sample - cover glass with emitters, 6) small magnets, 7) microscope objective, 8) coarse Z-positioner of the objective, 9) 45-deg mirror, 10) dichroic mirror, 11) steering mirror, 12) optional wide-field lens, 13) laser-line filter, 14) magnifying telescope with optional pinhole, 15) long-pass filters, 16) flip-mirror, 17) emCCD camera, 18) fibre-coupler, 19) multimode 50:50 fibre beam-splitter, 20, 21) coarse sample X,Y-positioner, 22) output multimode fibre.

Figure 39 shows a fluorescence image and the second order correlation function  $g^2(\tau)$  obtained from a single molecule (terrylene in a p-terphenyl crystal). The terrylene molecule is excited using total internal reflection. The  $g^2(\tau=0)$  value is around 0.2, which demonstrates the antibunching characteristic of the emitted photons. The maximum photon flux rate achieved with this setup using a single molecule is about 1 Mphoton/s.

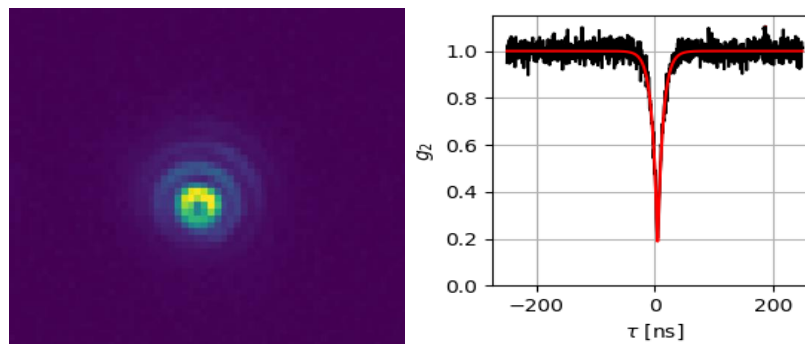


Figure 39. Left: Image of the fluorescence pattern of a single molecule (terrylene in p-terphenyl crystal). Right: Second order correlation function  $g^2(\tau=0)$ .

#### 4.4.6 Detection efficiency comparison

In this section, CMI, INRIM, NPL and PTB report on pilot studies for the measurements of detection efficiency of SPADs in the 1550 nm region, exploited a free-running InGaAs/InP SPAD-based detector.

Single-photon avalanche diodes (SPAD) based on InGaAs/InP semiconductor materials are the most exploited detectors in many quantum technologies [75, 76]. The successful development of such new technologies and products requires the solution to a number of metrological challenges; for this reason, a metrological characterisation in terms of detection efficiency, dead time, after pulsing and dark counts of single photon detectors is mandatory. A pilot study to compare different detection efficiency measurement strategies at the wavelength of 1550 nm was performed by four European National Metrology Institutes: CMI, INRIM, NPL and PTB [77]. The device under test was a commercial free-running fibre-coupled InGaAs/InP single-photon detector. The setup and the reference standard used as well as a detailed estimation of the measurement uncertainty of the detection efficiency was compared. The DUT was a fibre pigtailed free running SPAD (Id Quantique ID220), with nominal detection efficiency of 10 % and a dead time D of 10  $\mu$ s. All the participants

<sup>75</sup> Hadfield RH (2009) Nat Photonics 3:696–705

<sup>76</sup> Stucki D et al (2001) J Mod Opt 48(13):1967–1981

<sup>77</sup> Lopez M et al (2020) EPJ Quantum Technol. 7: 14

provided quantum efficiency measurement with the detector illuminated by a pulsed laser source, a commercial short-pulse laser source (ID Quantique, id300), which is based on a Distributed-feedback laser diode at 1550 nm. The measurement was carried out with the common repetition rate of 110 KHz. The exact wavelength of the source is measured with an optical spectrum analyser (Anritsu MS974 OA). The measurement principle used by all participating laboratories for determining the detection efficiency of the InGaAs/InP SPAD detector was based on the substitution method. In a general scheme, adopted by all the participants, the output of the laser was sent to a device that provide a variable calibrated attenuation to attenuate light at single photon level. The detection efficiency was estimated by comparing the optical power measured by the DUT with the incident mean optical power per laser pulse measured with an analogue calibrated detector.

A new model to evaluate efficiency in the presence of dead time and dark count effects of pulsed light illuminating a free-running detector was introduced and then extended to an extremely wide variety of experimental conditions [78]. The detection efficiency was measured by each NMI, in a range of mean photon number per pulse between 0.01 and 2.4, and standard uncertainty was reported. Results show consistency between the different measurement strategies.

#### 4.4.7 $g^{(2)}$ -comparison using Hanbury Brown Twiss interferometer

In this section, INRIM, PTB, NPL and CMI report on pilot studies for the measurements of source photon statistics for SPSs at telecom wavelength, together with an analogue comparison characterisation in the VIS-NIR regime, and the realisation of pilot measurement comparisons to validate the techniques developed. As a route to the validation of the measurement facilities and infrastructure, four European NMIs (INRIM, PTB, NPL and CMI) performed two joint measurements at INRIM labs of the Glauber second-order auto-correlation function ( $g^{(2)}$ ) of pseudo single-photon sources in two different configurations: CW heralded SPS at telecom wavelength [79] and NV-based SPS in pulsed excitation in the visible/near infrared [80]. Measurement protocols and procedures were developed on purpose.

The pilot study towards a comparison on the measurements of  $g^{(2)}$  in the telecom range [79] achieved a good agreement within the uncertainty. The source used for this test was a CW heralded single-photon source (HSPS) emitting real single photons at 1550 nm. In this experiment, every HBT is composed of two infrared InGaAs-InP SPADs. After a careful analysis of the setup parameters for a proper evaluation of the uncertainties associated to our measurements, INRIM, NPL and PTB obtained the results below (Table 6).

Table 6: Results of the  $g^{(2)}$  measurements in the telecom spectral range.

	$\alpha$ (INRIM)	$\alpha$ (NPL)	$\alpha$ (PTB)
INRIM-PTB	$0.016 \pm 0.006$	-	$0.04 \pm 0.05$
INRIM-NPL	$0.013 \pm 0.008$	$0.02 \pm 0.02$	-

As visible in the table above, the results of the whole measurement campaign (involving different measurement setups and data collection methodologies) are all in agreement within the experimental uncertainties reported (coverage factor:  $k = 1$ ).

Concerning the pilot study towards a comparison on the measurements of  $g^{(2)}(0)$  in the VIS-NIR regime [80], the source used was a pulsed single photon source based on nitrogen-vacancy centres in diamond. The validity of the technique is demonstrated by compatibility of the results obtained by the three partners (see Table 7), demonstrating a system-independent (and unaffected by the non-ideality of the apparatus), estimate of  $g^{(2)}(0)$ , emission lifetime ( $\tau = 15.34 \pm 0.08$  ns and their uncertainty).

Table 7: Results of the  $g^{(2)}$  measurements in the visible spectral range, using an NV-centre as the source.

	$\alpha$ (INRIM)	$\alpha$ (NPL)	$\alpha$ (PTB)
INRIM-PTB	$0.079 \pm 0.009$	-	$0.076 \pm 0.007$
INRIM-NPL	$0.065 \pm 0.005$	$0.068 \pm 0.005$	-

<sup>78</sup> Georgieva H et al (2021) Appl. Phys. Lett. 118, 174002

<sup>79</sup> Rebufello E et al (2019) Metrologia 56:025004

<sup>80</sup> E. Moreva et al. Metrologia 56, 015016 (2019)

#### 4.4.8 Summary and outlook

The consortium have developed the measurement capabilities in the European National Metrology Institutes with respect to the metrological characterisation and measurement traceability for single-photon sources significantly. These developments also triggered further developments in the metrology partner institutes. The setups and devices included detectors, detector characterisation setups, transportable single-photon sources, setups for the characterisation of the total spectral radiant flux and the photon statistics of single-photon sources as well as laser sources for the operation of single-photon sources.

## 5 Impact

This project will benefit end-users such as manufacturers of quantum communication systems, by giving them access to new and improved single-photon sources. NMIs can also use them as new standard sources for radiometry and photometry, enabling the NMIs to provide the measurements required to certify new quantum technologies based on the discrete and quantum properties of photons.

So far, the project has produced 46 peer reviewed, open access scientific publications and 121 conference presentations and posters, 9 presentations at an external seminar and events as well as 3 press releases. In addition, the project website is available at <https://www.sigust.eu/>

#### *Impact on industrial and other user communities*

The technological developments within this project support innovation in the field of quantum technologies, through the development of quantum devices for use in quantum communication and quantum metrology. More specifically, the single-photon sources (objectives 1, 2 & 3) and the supporting measurement infrastructure (objective 4) will help to develop the necessary measurement infrastructure for low photon flux measurements, i.e. new and better amplifiers and attenuators, new optical single photon excitation sources, which can be used in quantum communication, medicine, biology, and astronomy. The developed (standard) single-photon sources also have the potential to become a commercial product useful for companies active in the fields of quantum technology. This is particularly important as currently; the lack of useful single-photon sources hinders the development of quantum technology fields such as quantum cryptography and quantum metrology.

The project has compiled written training material for external audiences on “Ion-beam Engineering of Materials for Quantum Technologies”, which is available online at the International Atomic Energy Agency (IAEA) E-portal (<https://elearning.iaea.org/m2/course/index.php?categoryid=175>). The IAEA fosters international collaboration to help close currently existing gaps in physics, technology and regulation and the project’s information in the IAEA portal is freely available to end users such as those from industry.

In addition, press releases from the project have highlighted (i) the discovery of new properties of colour centres in diamond by UNITO researchers, (ii) the quantum revolution enabled by diamond defects and (iii) Metrology Common ground <https://www.nature.com/articles/s41567-019-0432-9.pdf>. The latter article discussed the development of the first standardised technique to characterise single-photon sources and how to provide common uncertainty estimation procedures to estimate the second-order correlation function, a parameter commonly used to describe single-photon sources.

#### *Impact on the metrology and scientific communities*

The project’s development of new standard sources based on single-photon emitters (objectives 1, 2 & 3) will support the realisation of optical radiant flux scales in the low-photon-flux region. It can also be used as the basis for the definition of the optical radiant flux in terms of photon rate, i.e. the countable number of photons over time, with selectable emission rates. As this field develops, it is expected that quantum standards, based on counting photons, will be used in radiometry and photometry and hence will impact metrology committees such as the Consultative Committee for Photometry and Radiometry (CCPR), EURAMET and COOMET.

The SI base unit for luminous intensity, covering the areas of photometry and radiometry, is the candela, which is currently realised in purely classical ways. This classical method involves either incandescent standard lamps carrying and maintaining the luminous intensity scale or photometers, which are radiometrically calibrated in a way which is traceable to the primary standard for optical radiant flux. In contrast, in the current

*mise en pratique* for the candela, the possibility for a photon-number-based realisation is explicitly formulated. Therefore, this project will contribute to the improvement of the *mise en pratique* for the candela.

This project's standard sources will also emit entangled photons (objective 3), thus supporting development in new fields in quantum metrology.

Currently, 1 PhD and 9 master theses were completed within the project, demonstrating transfer of knowledge to the next generation of scientists and metrologists.

Nine training courses within the consortium have also taken place to transfer knowledge between project partners. These training course topics included (i) single-photon sources based on quantum dots at 1550 nm (ii) single-photon sources based on quantum dots at 930 nm, (iii) single-photon sources based on single molecules, (iv) the installation of the portable single-photon source, (v) nitrogen-vacancy-assisted magnetic/electric field sensing, (vi) operation of SPS and PQED in a cryostat, (vii) operation of a 6-element transmission trap detector, (viii) single-photon devices based on electro-optical pumping, and (ix) traceable measurements of fibre coupled SPS photon flux. Further to this the project has provided five training courses to the external scientific community on, (i) single-photon sources based on defects in solid state, (ii) optical quantum metrology sensing and imaging in general, (iii) quantum encryption, (vi) ion-beam Engineering of Materials for Quantum Technologies, and (v) outcomes of the SIQUEST project (at the EURAMET TC-PR workshop).

Finally, the project has engaged with the scientific community by establishing 3 new collaborations, with Ruđer Bošković Institute (Croatia), the University of Leipzig (Germany) and the CNR-ISC (Italy).

#### *Impact on relevant standards*

The results of this project will provide input to new documentary standards in the field of low-flux radiometry, such as ETSI standards on quantum communication and quantum key distribution, and the *mise en pratique* for the candela. As mentioned above, the current *mise en pratique* for the candela allows the photon number based (and thus quantum based) realisation of photometric and radiometric units.

Recently, the project provided input to the CEN/CENELEC Focus Group on Quantum Technologies, in establishing a roadmap for standardisation in the field of quantum technologies. Further to this, the project has provided input to ETSI's Industry Specification Group on Quantum Key Distribution (ISG-QKD), where it contributed to the draft of ETSI GS QKD 013 "Characterisation of Optical Output of QKD transmitter modules", the DGS/QKD-0010\_IStrojan (GS QKD 010) "Implementation security against Trojan horse" and to an internal ISG Working Document to support the development of ETSI GS QKD 00.

#### *Longer-term economic, social and environmental impacts*

This project will have significant impact on the European market, by strengthening Europe's position in the field of quantum technologies. The single-photon sources and metrological infrastructure for traceable single-photon source characterisation developed within the project should support commercialisation and thus lead to better employment in high technology areas, due to the development of highly innovative devices for use in quantum technology fields (e.g. quantum cryptography), quantum communication, medicine, biology, and astronomy. In particular the field of data safety, guaranteed by secure quantum communication, will become ever more increasing important in all aspects of life for European citizens.

## 6 List of publications

1. Berchera, I. R.; Degiovanni, I. P. (2019): Quantum imaging with sub-Poissonian light: challenges and perspectives in optical metrology. In: *Metrologia* 56 (2), S. 24001. <https://doi.org/10.1088/1681-7575/aaf7b2>
2. Bernardi, E.; Moreva, E.; Traina, P.; Petrini, G.; Ditalia Tchernij, S.; Forneris, J. et al. (2020): A biocompatible technique for magnetic field sensing at (sub)cellular scale using Nitrogen-Vacancy centers. In: *EPJ Quantum Technology* 7, S. 13. <https://doi.org/10.1140/epjqt/s40507-020-00088-2>
3. Bradac, C.; Gao, W.; Forneris, J.; Trusheim, M. E.; Aharonovich, I. (2019): Quantum nanophotonics with group IV defects in diamond. In: *Nature Communications* 10 (1), S. 5625. <https://doi.org/10.1038/s41467-019-13332-w>
4. Bremer, L., Fischbach, S., Park, S.-I., Rodt, S., Song, J.-D., Heindel, T. and Reitzenstein, S. (2020), Cesium-Vapor-Based Delay of Single Photons Emitted by Deterministically Fabricated Quantum Dot Microlenses. *Adv. Quantum Technol.*, 3: 1900071. <https://doi.org/10.1002/qute.201900071>

5. Bremer, L.; Weber, K.; Fischbach, S.; Thiele, S.; Schmidt, M.; Kaganski, A. et al. (2020): Quantum dot single-photon emission coupled into single-mode fibers with 3D printed micro-objectives. In: *APL Photonics* 5 (10), S. 106101. <https://doi.org/10.1063/5.0014921>
6. Christinck, J., Rodiek, B., López, M. et al. Characterization of the angular-dependent emission of nitrogen-vacancy centers in nanodiamond. *Appl. Phys. B* 126, 161 (2020). <https://doi.org/10.1007/s00340-020-07508-2>
7. Colautti, M., Lombardi, P., Trapuzzano, M., Piccioli, F.S., Pazzagli, S., Tiribilli, B., Nocentini, S., Cataliotti, F.S., Wiersma, D.S. and Toninelli, C. (2020), A 3D Polymeric Platform for Photonic Quantum Technologies. *Adv. Quantum Technol.*, 3: 2000004. <https://doi.org/10.1002/qute.202000004>
8. Ditalia Tchernij, S.; Lüthmann, T.; Corte, E.; Sardi, F.; Piccolo, F.; Traina, P. et al. (2020): Fluorine-based color centers in diamond. In: *Scientific Reports* 10 (1), S. 21537. <https://doi.org/10.1038/s41598-020-78436-6>
9. Ditalia Tchernij, S.; Lüthmann, T.; Herzig, T.; Küpper, J.; Damin, A.; Santonocito, S. et al. (2018): Single-Photon Emitters in Lead-Implanted Single-Crystal Diamond. In: *ACS Photonics* 5 (12), S. 4864–4871. <https://doi.org/10.1021/acsp Photonics.8b01013>
10. Georgieva, H.; López, M.; Hofer, H.; Christinck, J.; Rodiek, B.; Schnauber, P.; Kaganskiy, A.; Heindel, T.; Rodt, S.; Reitzenstein, S.; Kück, S. (2020): Radiometric characterization of a triggered narrow-bandwidth single-photon source and its use for the calibration of silicon single-photon avalanche detectors. In: *Metrologia* 57 055001. <https://doi.org/10.1088/1681-7575/ab9db6>
11. Forneris, J.; Ditalia Tchernij, S.; Traina, P.; Moreva, E.; Skukan, N.; Jakšić, M. et al. (2018): Mapping the Local Spatial Charge in Defective Diamond by Means of NV Sensors - A Self-Diagnostic Concept. In: *Physical Review Applied* 10 (1). <https://doi.org/10.1103/PhysRevApplied.10.014024>; <https://arxiv.org/abs/1706.07935>
12. Görlitz, J.; Herrmann, D.; Thiering, G.; Fuchs, P.; Gandil, M.; Iwasaki, T. et al. (2020): Spectroscopic investigations of negatively charged tin-vacancy centres in diamond. In: *New Journal of Physics* 22 (1), S. 13048. <https://doi.org/10.1088/1367-2630/ab6631>
13. Huber, D.; Lehner, B. U.; Csontosová, D.; Reindl, M.; Schuler, S.; Covre Da Silva, S. F. et al. (2019): Single-particle-picture breakdown in laterally weakly confining GaAs quantum dots. In: *Physical Review B* 100 (23). <https://doi.org/10.1103/PhysRevB.100.235425>
14. Llorens, J. M.; Lopes-Oliveira, V.; López-Richard, V.; Oliveira, E. CardozoR. de; Wewiór, L.; Ulloa, J. M. et al. (2019): Topology Driven g-Factor Tuning in Type-II Quantum Dots. In: *Physical Review Applied* 11 (4), S. 44011. <https://doi.org/10.1103/PhysRevApplied.11.044011>; <https://arxiv.org/abs/1710.08828>
15. Lombardi, P.; Trapuzzano, M.; Colautti, M.; Margheri, G.; Degiovanni, I. P.; López, M. et al. (2019): A Molecule-Based Single-Photon Source Applied in Quantum Radiometry. In: *Advanced Quantum Technologies* 3 (2), S. 1900083. <https://doi.org/10.1002/qute.201900083>
16. López, M.; Meda, A.; Porrovecchio, G.; Starkwood, R. A.; Genovese, M.; Brida, G. et al. (2020): A study to develop a robust method for measuring the detection efficiency of free-running InGaAs/InP single-photon detectors. In: *EPJ Quantum Technology* 7 (1), S. 14. <https://doi.org/10.1140/epjqt/s40507-020-00089-1>
17. Marletto, C.; Vedral, V.; Virzi, S.; Rebufello, E.; Avella, A.; Piacentini, F. et al. (2019): Theoretical description and experimental simulation of quantum entanglement near open time-like curves via pseudo-density operators. In: *Nature Communications* 10 (1), S. 1–7. <https://doi.org/10.1038/s41467-018-08100-1>
18. Moreva, E.; Bernardi, E.; Traina, P.; Sosso, A.; Tchernij, S. D.; Forneris, J. et al. (2020): Practical Applications of Quantum Sensing: A Simple Method to Enhance the Sensitivity of Nitrogen-Vacancy-Based Temperature Sensors. In: *Physical Review Applied* 13 (5), S. 54057. <https://doi.org/10.1103/PhysRevApplied.13.054057>; <https://arxiv.org/abs/1912.10887>
19. Moreva, E.; Traina, P.; Kirkwood, R. A.; López, M.; Brida, G.; Gramegna, M. et al. (2019): Feasibility study towards comparison of the  $g(2)(0)$  measurement in the visible range. In: *Metrologia* 56 (1), S. 15016. <https://doi.org/10.1088/1681-7575/aaf6c8>
20. Nawrath, C.; Olbrich, F.; Paul, M.; Portalupi, S. L.; Jetter, M.; Michler, P. (2019): Coherence and indistinguishability of highly pure single photons from non-resonantly and resonantly excited telecom C-band quantum dots. In: *Applied Physics Letters* 115 (2), S. 23103–23105. <https://doi.org/10.1063/1.5095196>
21. Petrini, G.; Moreva, E.; Bernardi, E.; Traina, P.; Tomagra, G.; Carabelli, V. et al. (2020): Is a Quantum Biosensing Revolution Approaching? Perspectives in NV-Assisted Current and Thermal Biosensing in Living Cells. In: *Advanced Quantum Technologies*, S. 2000066. <https://doi.org/10.1002/qute.202000066>
22. Rebufello, E.; Piacentini, F.; López, M.; Kirkwood, R. A.; Ruo Berchera, I.; Gramegna, M. et al. (2019): Towards a standard procedure for the measurement of the multi-photon component in a CW telecom heralded single-photon source. In: *Metrologia* 56 (2), S. 25004. <https://doi.org/10.1088/1681-7575/ab022e>

23. Schimpf, C.; Reindl, M.; Klenovský, P.; Fromherz, T.; Covre Da Silva, S. F.; Hofer, J. et al. (2019): Resolving the temporal evolution of line broadening in single quantum emitters. In: *Optics Express* 27 (24), S. 35290. <https://doi.org/10.1364/OE.27.035290>
24. Schmidt, R.; Schmidt, M.; Helversen, M. V.; Fischbach, S.; Kaganskiy, A.; Schliwa, A. et al. (2019): Deterministically fabricated spectrally-tunable quantum dot based single-photon source. In: *Optical Materials Express* 10 (1), S. 76. <https://doi.org/10.1364/OME.10.000076>
25. Steindl, P.; Sala, E. M.; Alén, B.; Marrón, D. F.; Bimberg, D.; Klenovský, P. (2019): Optical response of (InGa)(AsSb)/GaAs quantum dots embedded in a GaP matrix. In: *Physical Review B* 100 (19). <https://doi.org/10.1103/PhysRevB.100.195407>; <https://arxiv.org/abs/1906.09842>
26. Virzi, S.; Rebufello, E.; Avella, A.; Piacentini, F.; Gramegna, M.; Ruo Berchera, I. et al. (2019): Optimal estimation of entanglement and discord in two-qubit states. In: *Scientific Reports* 9 (1), S. 1–9. <https://doi.org/10.1038/s41598-019-39334-8>
27. Żołnacz, K.; Musiał, A.; Srocka, N.; Große, J.; Schlöisinger, M. J.; Schneider, P.-I. et al. (2019): Method for direct coupling of a semiconductor quantum dot to an optical fiber for single-photon source applications. In: *Optics Express* 27 (19), S. 26772. <https://doi.org/10.1364/OE.27.026772>
28. Gajjela, R.S.R., Hendriks, A.L., Douglas, J.O. et al. Structural and compositional analysis of (InGa)(AsSb)/GaAs/GaP Stranski–Krastanov quantum dots. *Light Sci Appl* 10, 125 (2021). <https://doi.org/10.1038/s41377-021-00564-z>; <https://www.nature.com/articles/s41377-021-00564-z#Abs1>
29. Steindl, P., et al. On the importance of antimony for temporal evolution of emission from self-assembled (InGa)(AsSb)/GaAs quantum dots on GaP(001), *New J. Phys.* 23 103029 (2021). <https://doi.org/10.1088/1367-2630/ac2bd6>
30. Ditalia Tchernij, S., Lühmann, T., Corte, E. et al., Fluorine-based color centers in diamond. *Sci Rep* 10, 21537 (2020). <https://doi.org/10.1038/s41598-020-78436-6>
31. Ditalia Tchernij, S., et al., Spectral features of Pb-related color centers in diamond – a systematic photoluminescence characterization, *New J. Phys.* 23 063032 (2021), <https://doi.org/10.1088/1367-2630/ac038a>
32. Corte, E., Sachero, S., Ditalia Tchernij, S., Lühmann, T., Pezzagna, S., Traina, P., Degiovanni, I.P., Moreva, E., Olivero, P., Meijer, J., Genovese, M. and Forneris, J., Spectral Emission Dependence of Tin-Vacancy Centers in Diamond from Thermal Processing and Chemical Functionalization. *Adv. Photonics Res.*, 3: 2100148 (2022). <https://doi.org/10.1002/adpr.202100148>
33. Picollo, F., et al., Creation of pure non-crystalline diamond nanostructures via room-temperature ion irradiation and subsequent thermal annealing, *Nanoscale Advances* 3, 4156-4165 (2021) <https://doi.org/10.1039/D1NA00136A>
34. Georgieva, H., Marco López, Helmuth Hofer, Niklas Kanold, Arsenty Kaganskiy, Sven Rodt, Stephan Reitzenstein, and Stefan Kück, "Absolute calibration of a single-photon avalanche detector using a bright triggered single-photon source based on an InGaAs quantum dot," *Opt. Express* 29, 23500-23507 (2021), <https://doi.org/10.1364/OE.430680>
35. Hirt, F., et al., Sample fabrication and metrological characterization of single-photon emitters based on nitrogen vacancy centers in nanodiamonds, *Eng. Res. Express* 3 045038 (2021), <https://doi.org/10.1088/2631-8695/ac34c2>
36. Christinck, J., et al., Comparison of back focal plane imaging of nitrogen vacancy centers in nanodiamond and core-shell CdSe/CdS quantum dots, *J. Phys.: Conf. Ser.* 2149 012014 (2022), <https://doi.org/10.1088/1742-6596/2149/1/012014>
37. Kück, S., Single photon sources for absolute radiometry – A review about the current state of the art, *Measurement: Sensors* 18, 100219 (2021), <https://doi.org/10.1016/j.measen.2021.100219>
38. Fuchs, P., Thomas Jung, Michael Kieschnick, Jan Meijer, and Christoph Becher, "A cavity-based optical antenna for color centers in diamond", *APL Photonics* 6, 086102 (2021), <https://doi.org/10.1063/5.0057161>
39. Rebufello, E., Piacentini, F., Avella, A. et al. Anomalous weak values via a single photon detection. *Light Sci Appl* 10, 106 (2021). <https://doi.org/10.1038/s41377-021-00539-0>
40. Rebufello, E.; Piacentini, F.; Avella, A.; Lussana, R.; Villa, F.; Tosi, A.; Gramegna, M.; Brida, G.; Cohen, E.; Vaidman, L.; Degiovanni, I.P.; Genovese, M. Protective Measurement—A New Quantum Measurement Paradigm: Detailed Description of the First Realization. *Appl. Sci.* 2021, 11, 4260. <https://doi.org/10.3390/app11094260>
41. Lombardi, P., Maja Colautti, Rocco Duquennoy, Ghulam Murtaza, Prosenjit Majumder, and Costanza Toninelli, "Triggered emission of indistinguishable photons from an organic dye molecule", *Appl. Phys. Lett.* 118, 204002 (2021), <https://doi.org/10.1063/5.0048567>
42. Duquennoy, R., et al., Real-time two-photon interference from distinct molecules on the same chip, *Optica*, <https://arxiv.org/abs/2201.07140>

43. Kück, S., López, M., Hofer, H. et al. Single photon sources for quantum radiometry: a brief review about the current state-of-the-art. Appl. Phys. B 128, 28 (2022). <https://doi.org/10.1007/s00340-021-07734-2>
44. Rodt, S., Reitzenstein S., High-performance deterministic in situ electron-beam lithography enabled by cathodoluminescence spectroscopy, Nano Express 2, 014007 (2021). <https://doi.org/10.1088/2632-959X/abed3c>
45. M. Schmidt et al., Bimodal behavior of microlasers investigated with a two-channel photon-number-resolving transition-edge sensor system, Physical Review Research 3, 013263 (2021). <https://doi.org/10.1103/PhysRevResearch.3.013263>
46. Laiho, K. et al., Photon-number parity of heralded single photons from a Bragg-reflection waveguide reconstructed loss-tolerantly via moment generating function, New Journal of Physics 21, 103025 (2019). <https://doi.org/10.1088/1367-2630/ab42ae>

This list is also available here: <https://www.euramet.org/repository/research-publications-repository-link/>

## 7 Contact details

Coordinator:

Stefan Kück, PTB

Tel: +49 531 5924010

E-mail: [stefan.kueck@ptb.de](mailto:stefan.kueck@ptb.de)

Project website address: <https://www.siqust.eu/>